# Mechanics, Dynamics and Thermal Analysis of Hard Turning Process

by

Kıvılcım Büyükhatipoğlu

A Thesis Submitted to the
Graduate School of Engineering
in Partial Fulfillment of the Requirements for
the Degree of

Master of Science

in

Mechanical Engineering

Koç University

July 2004

Koc University

Graduate School of Sciences and Engineering

This is to certify that I have examined this copy of a master's thesis by

Kıvılcım Büyükhatipoğlu

and have found that it is complete and satisfactory in all respects,

and that any and all revisions required by the final

examining committee has been made.

Committee Members:

İsmail Lazoğlu, Ph. D. (Advisor)

Murat Sözer, Ph. D.

Erhan Budak, Ph. D.

Date: 29.07.2004

## ABSTRACT

In precision machining, due to the recent developments on the cutting tools, machine tool structural rigidity and improved CNC controllers, hard turning is an emerging process as an alternative to some of the grinding processes by providing reductions in costs and cycle-times. In industrial environments, hard turning is established for geometry features of parts with low to medium requirements on part quality. Better and deeper understanding of cutting forces, stresses and temperature fields, temperature gradients created during the machining are very critical for achieving highest quality products and high productivity in feasible cycle times.

In order to enlarge the capability profile of the hard turning process, this thesis introduces to prediction models of mechanical and thermal loads during turning of 51CrV4 with hardness of 68 HRC by CBN tool. The shear flow stress, shear and friction angles are determined from the orthogonal cutting tests. Cutting force coefficients are determined from orthogonal to oblique transformations. Cutting forces, temperature field of chip, tool and workpiece are predicted and compared with experimental measurements. The experimental temperature measurements are conducted by the advanced hardware device FIRE-1 (Fiberoptic Ratio Pyrometer).

## ACKNOWLEDGEMENTS

I would like to express my sincere gratitude and appreciation to my advisor, Dr. Ismail Lazoglu for his expert guidance and mentorship and I would also like to thank Dr. Murat Sozer and Dr. Erhan Budak for reading this dissertation and offering constructive comments.

I would like to acknowledge Prof. Dr. F. Klocke and Diplom Ing. H. Kratz from WZL, Aachen University of Technology for their support on this collaborative research, and Renault-Nissan Company and Element Six Ltd. for the information on material properties.

I would also like to thank all of my friends, particularly to Muge Pirtini, Mert Sasoglu, Isil Yildirim, and Isilay Talay Degirmenci for making these two years more pleasant and their presence when I needed. Without them this thesis could not have been completed.

And finally, I would like to thank to my family, especially to my mother Atiye Buyukhatipoglu and my father Haluk Buyukhatipoglu for their life-long love, for the kind of encouragement and support they have provided me throughout my entire education life, and for their absolute confidence in me. This thesis and my all previous success are dedicated to them.

## TABLE OF CONTENTS

## LIST OF TABLES

## LIST OF FIGURES

## NOMENCLATURE

| | |
|---|---|
| $\alpha_n, \beta_n$ | Normal rake and normal friction angles |
| $\alpha_p, \alpha_f, \psi_r$ | Back rake, side rake and side cutting edge angles |
| $\alpha_0$ | Orthogonal rake angle |
| $\eta$, i | Chip flow angle and inclination angle |
| $\phi_r, \phi_f$ | Transfer function along the radial and feed directions |
| r, $\psi$ | Radial distance and angular position |
| $\delta x, \delta y, \delta r, \delta\psi$ | Grid lengths in x, y, radial and angular directions |
| $\theta$ | Cutter rotation angle |
| c, $\rho$, $\zeta$ | Specific heat capacity, density and thermal diffusivity |
| $\tau, \phi_n$ | Shear stress and shear angle |
| $\omega_{ni}, k_i, \zeta_i$ | Natural frequency, stiffness and damping ratio for the $i^{th}$ mode |
| $\chi$ | Proportion of shearing heat entering into the workpiece |
| $B_i$ | Proportion of frictional heat entering into the tool in the $i^{th}$ nodal point |
| c, h | Feed per revolution and uncut chip thickness |
| $K_{tc}, K_{fc}, K_{rc}$ | Tangential, feed, radial cutting force coefficients |
| $K_{te}, K_{fe}, K_{re}$ | Tangential, feed, radial edge force coefficients |
| $dF_t, dF_r, dF_f$ | Differential tangential, radial and feed forces |
| $P_c, T_c$ | Total cutting torque and power |
| n | Spindle revolution |
| D | Diameter of the turned shaft |
| $a_d, \bar{a}, \tilde{a}$ | Actual, intended and dynamic radial depth of cuts |
| $c_d, \bar{c}, \tilde{c}$ | Actual, intended and dynamic feed rates |
| $F_f, F_s$ | Friction and shear forces |

| | |
|---|---|
| $k_t, k_c$ | Thermal conductivity of the tool and chip |
| $l, l_{cn}$ | Shear plane and tool-chip contact length |
| $N_x, N_y, N_z$ | Number of grids along x, y, z axis |
| $N_p$ | Number of angular grids |
| $\dot{Q}_c$ | Frictional heat flow into chip control zone |
| $\dot{Q}_t$ | Heat generation rate per unit area |
| $R_t$ | Thermal number |
| $\dot{Q}_s, \dot{Q}_f$ | Energy generated in shear and along tool chip contact |
| $T_w, T_c, T_t$ | Workpiece, chip and tool temperature arrays |
| $V_w, V_c, V_s$ | Cutting, chip and shear velocities |

# Chapter 1

## INTRODUCTION

The vast majority of hard components used in the automotive industry are machined to final geometrical form after hardening. Currently, grinding, which involve expensive machinery and have long manufacturing cycles, costly support equipment, and lengthy setup times, is the predominant method for finishing these parts, which include bearings, gears, shafts, and pinions. After the improvements in machine tool rigidity and the development of polycrystalline cubic boron nitride (PCBN) cutting tools, hard turning, which is best performed with appropriately configured turning centers or lathes, becomes as a cost-effective alternative to grinding. Hard turning is defined as the process of single point cutting of part pieces that have hardness values over 45 HRC. Typically, however, hard turned part pieces will be found to lie within the range of 58-68 HRC.

Hard turning is best accomplished with cutting inserts made from either CBN (Cubic Boron Nitride), Cermet or Ceramic. A properly configured machine tool and the appropriate tooling are required in high quality hard turning applications. Although grinding is known to produce good surface finish at relatively high feed rates, hard turning using CBN inserts can produce as good or better surface finish at significantly higher material removal rates if the proper combination of tool, insert nose radii, feed rate or the new wiper insert technology is utilized. A properly configured hard turning cell would typically demonstrate surface finishes of approximately 0.003 mm and roundness values of about 0.00025 mm.

Hard turning is an important technology because all manufacturers are continually seeking ways to manufacture their parts with lower cost, higher quality, rapid setups, lower investment, and smaller tooling inventory. The migration of processing from grinders to lathes can satisfy each and every one of these goals.

On a daily basis, parts are being hard turned in the following industry segments; automotive, bearing, marine, punch and die, mold, hydraulics and pneumatics, machine tool and aerospace. While these industries are representative, this list is certainly not conclusive and new applications and industry segments are constantly being added. Commonly processed hard turned materials would include steel alloys such as bearing steels, hot and cold work tool steels, high speed steels, die steels and case hardened steels.

With hard turning, cost of the process is reduced in many ways. First of all, a CNC lathe is a much smaller investment than a grinder. Also, CNC lathes are much more flexible in terms of machining capabilities. Low maintenance is also a benefit, as worn PCBN tools may be quickly removed and replaced with new inserts, and do not require truing or dressing to maintain the cutting profile. Moreover, while PCBN tools can cost up to 10 to 20 times more than conventional tools, studies have shown them to be 10 to 300 times more effective in terms of overall productivity and tool life. CNC lathes also take up less floor space than grinders, and they do not even require coolant. Like all new manufacturing processes, hard turning is technology-driven. The factors that influence the hard turning process can be categorized into the main topics of machine construction, process, work holding, materials, heat treat and tooling.

Therefore, in precision machining, due to the recent developments on the cutting tools, machine tool structural rigidity and improved CNC controllers, hard turning is an emerging process as an alternative to some of the grinding processes by providing reductions in costs and cycle-times. In industrial environments, hard turning is established for geometry features of parts with low to medium requirements on part quality. Better and deeper understanding of cutting forces, stresses, temperature fields, and temperature gradients created during the machining are very critical for achieving highest quality products and high productivity in feasible cycle times.

In order to enlarge the capability profile of the hard turning process, in this thesis, prediction models of mechanical and thermal loads during turning of 51CrV4 with hardness of 68 HRC by CBN tool are introduced.

Chapter 2 provides the necessary background and literature review on hard turning process. The fundamentals of metal cutting analysis, cutting mechanics, previous models for prediction of cutting forces, temperature fields and residual stresses in orthogonal turning and hard turning process are reviewed.

In Chapter 3, after a brief introduction to turning process is given for making the reader more familiar with the definitions used in hard turning process, the proposed mechanical approach for predicting the cutting forces is explained. Calibration process details are also given in this chapter, where the method of determining cutting constants for the force model is described. Validation tests performed in order to validate the accuracy of the proposed model under various test conditions are described and tests results are given together with the comparison of the experimental and predicted cutting force values.

In Chapter 4, a process model is developed for prediction of dynamic cutting forces and surface errors in hard turning. The resultant surface profile is compared with the experimental data obtained from surface roughness measurements.

In Chapter 5, tool, chip, and workpiece temperature fields in hard turning operation are predicted by using a numerical model based on finite difference method. The predicted temperature fields are compared with the thermal measurements obtained by using Fire-1 Fiber-optic Ratio Pyrometer. In order to validate the model for other cutting conditions and materials, simulations were also performed on aluminum parts and the results are compared with the results in literature.

The thesis is concluded with a short summary of the performed study and future work.

# Chapter 2

## LITERATURE REVIEW

Surface finish operations of hardened steels with the hardness of near or above 60 HRC is becoming quite attractive alternatives to the grinding processes nowadays. This has been enabled with the advancements of the Cubic Boron Nitride (CBN) tools. In addition to the developments on the cutting tools, recent improvements on machine tool structural rigidity and on the CNC controllers that allowed submicron programming helped the hard turning processes to be realized. Hard turning process is best performed with appropriately configured turning centers or lathes. In his papers, Koenig [1] discusses the characteristics of hard machined surfaces especially of white layers. Furthermore, the development in the area of high precision machining of hardened steels is presented. Hard turning processes generally takes less cycle time, requires fewer operations, have lower costs and higher material removal rate. Hard turning also fits with the current manufacturing trends in which production flexibility and part consistency are two important distinctions ([1], [4]).

Although the practical applications of hard turning in various industries have been started for some time ago, unfortunately the fundamental scientific and engineering issues, such as cutting forces, temperatures, and residual stresses in hard turning processes have not been very well understood yet. Ko and Kim [5] investigated the feasibility of internal intermittent hard turning. Their research showed that intermittent hard turning can produce surface integrity which is good enough for replacing the grinding process. Scheffer et al. [6] describes an in-depth study on the development of a system for monitoring tool wear in hard turning. Various aspects associated with hard turning were investigated with the aim of designing an accurate tool wear-monitoring system for hard turning. Narutaki and Yamane [7] tested sintered CBN tools to evaluate the cutting performance and cutting temperature in machining of variously heat-treated tool steels, case hardening steels, and high-speed steels. They have also conducted diffusion tests between steel and CBN tool to ascertain the thermo-chemical wear of CBN tools. In his dissertation, Koch [8] discusses the importance of early tool wear, tool breakage, chipping, residual stresses, white layer phenomena, machined surface quality and surface integrity of hard turning processes in industrial applications.

Ng et al. [9] briefly reviewed the development of analytical models of the cutting process, including more recent work involving finite element (FE) methods for temperature and force calculation in orthogonal hard turning. Details of the different FE packages and formulation methods used by different researchers were given. Wang and Liu [10] measured the cutting forces and utilized them to predict the interface temperature. Their thermal model was based on Green's function and a microstructure-based method using orthogonal hard turning. Moreover, currently available literature on hard turning is focusing mostly on the experimental evaluation of the process, especially on the subjects of chip morphology, chip formation, machinability and tool wear. Davies et al. [11] investigated the factors affecting tool wear and the mechanics of the chip formation process in finish hard turning process performed by CBN tools. Shaw and Vyas [12] investigated chip formation in the machining of hardened steel. They reviewed cyclic saw toothed type chip formation which is formed during the machining operation of gears using PCBN tools. Tool nose radius effects on finish turning of hardened AISI 52100 steels have been investigated by Chou and Song [13]. They have evaluated surface finish, tool wear, cutting forces, and, particularly, white layer at different machining conditions. Poulachon et al. [14] investigated the tool-wear mechanisms of CBN cutting tools in finish turning of the AISI D2 cold work steel, AISI Hll hot work steel, 35NiCrMo16 hot work steel and AISI 52100 bearing steel. A large variation in tool-wear rate has been observed in machining of these steels. The generated tool flank grooves have been correlated with the hard carbide content of the workpieces. The influence of feed rate, cutting speed, and tool wear on the process of hard turning of case-hardened 27MnCr5 gear conebrakes is examined by Rech and Moisan [15], and technical limitations in mass production are pointed out. In this work, cutting temperatures obtained in the process were studied using a mixed experimental and numerical approach. Ren et al. [16] studied cutting temperatures of hardfacing materials by using remote thermocouple technique and finite element (FE) simulation. Mamalis et al. [17] constructed an equivalent thermo-mechanical plane-strain orthogonal cutting model based on the real turning chip cross-section, coming from the nominal values of tool nose radius, feed and depth of cut, with mean representative values of depth and width of cut, by employing a commercial FE code.

Significant research has been performed in conventional turning for mathematical process modeling. Ehmann et al. [18] presented a summary of work performed in the area of modeling of the dynamic metal cutting process. Four modeling approaches including analytical, experimental, mechanistic and numerical methods were critically reviewed. A brief assessment of future research needs was also given. Luttervelt et al. [19] discussed the present situation and future trends in modeling of machining operations in their paper. They presented a progress report of the CIRP working group, 'Modeling of Machining Operations', based on information obtained from the members of the working group, from consultation in industry, study of relevant literature and discussions at meetings of the working group with the aim to stimulate and pilot future developments.

Tobias and Fishwick [20], and Tlusty and Polacek [21] were among the few early researchers to study dynamic cutting. They explained the fundamental mechanism of chatter during turning and derived the stability theory which analytically predicts chatter free cutting conditions. Their theory was based on the orthogonal cutting model where the directions of cutting forces and the structural dynamics of the cutter-workpiece system were assumed constant. Lazoglu et al. [22] presented a mathematical model and a computational algorithm for the time domain solution of boring process dynamics. The model was developed in a modular form; it included a workpiece geometry and surface topography module, a kinematics and tool position module, a dynamic chip load module, a dynamic cutting force prediction module and a structural dynamics module. The time domain model took cutting process parameters, tool and workpiece geometries and modal parameters of the structure as inputs. It predicted instantaneous cutting forces and vibrations along the machining time, and machined workpiece topography as outputs. Some of the simulated and experimental results for various cutting conditions were presented and they showed good agreement.

The history of cutting temperature research goes back as early as Taylor's experimental works. His research showed that tool life decreases when cutting speed increases. Triger and Chao [23] were the first researches evaluating the cutting temperature analytically. They have performed the average tool-chip interface temperature calculations and found that plastic deformation associated with chip formation at the shear zone, and friction between the tool and chip affects the temperature distribution. A simple analytical model computing the interface temperature by assuming the tool as a quarter-infinite body was developed by Loewen and Shaw [24]. Usui et al. [25] and Tlusty et al. [26] used finite difference method to predict the steady state temperature distribution in continuous machining. They had found that the experimental temperatures were higher than the predicted ones near the cutting edge and the chip leaving point. They correlated the crater wear of carbide tools to the predicted temperature and stresses in the tool. Smith and Armarego [27] presented a three-dimensional temperature analysis for classical orthogonal cutting operations based on the thin shear zone model, popular shear zone temperature equations, and finite difference techniques. Ren and Altintas [28] applied slip line field solution proposed by Oxley [29] on high speed orthogonal turning of hardened mold steels with chamfered carbide and CBN tools. Shatla et al. [30] used material properties evaluated from orthogonal cutting and milling tests on Finite Element simulation of temperature. Strenkowski and Moon [31] developed an Eularian Finite Element model to simulate the temperature. Finite element methods require accurate representation of material's constitutive properties during machining; therefore they mainly suffer due to lack of accurate material models. Sukaylo et al. [32] presented novel theoretical and experimental solutions to establish parameters of a finite element method-based computer model, developed for the simulation of thermal deformation in multi-pass turning. Huang and Liang [33] analytically modeled the thermal behaviors of the primary and the secondary heat sources by using Oxley's predictive machining theory. Workpiece material property is represented as a function of strain, strain rate, and temperature by using a modified Johnson-Cook equation. Redulescu and Kapoor [34] analyzed the tool-chip interface temperature by solving the heat conduction problem with prescribed heat flux. The mechanistic force model was utilized in this analysis. Their results also indicate that the tool-chip interface temperature increases with cutting speed for both continuous and interrupted cutting. Jen and Lavine [35] used a similar approach to Redulescu for tool temperature calculation and they improved calculation speed relatively by using power law approximation for the exponential terms. For further information on the literature review and on methods to calculate the machining temperature, the publication by Tay [36] is recommended.

One of the biggest challenges in this research area is the lack of experimental data to verify the mathematical models proposed in predicting the cutting temperature. It is hard to embed sensors close to the cutting edge of the rotating tool. Most published articles rely on the few published experimental data from Trigger and Chao [23], Boothroyd [37] and Stephenson et al. [38]. In his paper, Boothroyd presented the results of a photographic technique for the determination of the complete temperature distribution in the orthogonal metal cutting process. He showed that the results disagree with the previous theoretical results. The temperatures along the tool rake face are of particular interest because they affect the wear of the cutting tool and friction between the tool and the chip.

In the past, causes of the residual stress have been attributed to mechanical and thermal loads on the workpiece. Henriksen [39] had studied the stress inducing effect of single point tools working in steels and developed methods for computing the stresses induced. Methods of investigation were described and data was given for stresses produced in various materials, by various tools, and under various cutting conditions. According to his research, in ductile materials the stresses are, generally, tensile, and in cast iron they are compressive. He suggested that the mechanical force on the tool is the primary cause and the thermal stress is negligible. Okushima and Kakino [40] suggested that residual stress in the machined surface is caused by the ploughing force at the tool edge and thermal effect of temperature distribution produced in cutting. Residual stresses were calculated by using finite element method and compared with those measured by X-Ray diffraction technique. Liu and Barash [41] studied mechanical residual stresses in a machined surface experimentally. They concluded that in orthogonal cutting, length of shear plane, tool flank wear, the shape of cutting edge, and the depth of cut determine the pattern of residual stresses. Residual stresses near the machined surface were found to be determined by the shape of the cutting edge, such as edge radius, and effective clearance angle. They observed that smaller depth of cuts can also end up with high tensile stresses near the surface.

Merwin and Johnson [42] studied on the plastic deformation in rolling contact and on the basis of an idealized material which was elastic-perfectly plastic and isotropic, and they showed that complex cycle of stress and strain encountered in rolling causes a forward displacement of the surface. During the first few cycles of the load, compressive residual stresses were introduced in the subsurface layers. Jiang and Sehitoglu [43] developed an analytical approach for approximate determination of residual stresses and strain accumulation in elastic-plastic stress analysis of rolling contact. Their model constituted a significant improvement over the Merwin-Johnson's model. Subsurface residual stresses were determined by the normal load and the influence of the tangential force penetrated to % 15 of the contact area.

Matsumato and Wu [44] performed an analysis which was based on the existence of several measurable factors that influence the stress field in machined material during cutting. They had performed the analysis in two stages. The effects of hardness on several process related factors and the roles of these factors in residual stress formation were then investigated through mechanical and thermal analysis. Shear angle was found to increase with material hardness and this made residual stress on the machined surface more compressive. Temperature rise made the residual stresses more tensile and as hardness was increased, more tensile residual stresses were obtained because of the increased yield point. These competing effects governed residual stress formation.

Jang and Seireg [45] discussed the development of a computer based simulation of the machine-workpiece interaction during the turning process. They developed a model to study the influence of system parameters on the generated surface roughness. These analytical results showed good agreement with published experimental data relating the roughness to machine tool stiffness, tool vibration frequency, feed, speed, depth of cut, and tool cutting edge radius. For prediction of machining induced residual stresses, Jang and Seireg [46] developed an analytical model. Shih [47] developed a plane-strain finite element method for the simulation of orthogonal metal cutting with continuous chip formation. Effects of elasticity, viscoplasticity, temperature, large strain, and high strain-rate, were used to simulate the material deformation during the cutting process. The deformation of the finite element mesh was presented and residual stress distributions were compared with the X-ray diffraction measurements.

Mittal and Liu [48] also developed a model proposing that the residual stress profile is a deterministic function of the machining parameters. Residual stress profile along the depth was assumed as a polynomial function of the depth and the coefficients of the polynomial were assumed to be as functions of the machining parameters. The underlying assumption in the entire model was that residual stresses produced by identical conditions are also identical. To check this assumption, different specimens were machined using the same cutting conditions. By this way, an experimental model which was predicting the residual stresses in precision hard turning was introduced. Mahdi and Zhang [49] developed a numerical method to appropriately accommodate the phase transformation in a workpiece experiencing critical temperature variation during grinding. They found that if material properties are temperature independent, residual stresses created are tensile, however if they are temperature dependent, surface hardening occurs when temperature raises, and maximum residual stress increases. Chen et al. [50] found that thermal stresses generated in grinding process were the primary cause of tensile residual stresses and they are strongly dependent on workpiece material properties. Walsh et al. [51] proposed a model of the formation of thermally induced tensile residual stresses and developed a simple method for calculating critical temperature above which tensile residual stresses occur. The model was then validated using finite element techniques. Thiele et al. [52] conducted an experimental investigation to determine the effects of tool cutting edge geometry and workpiece hardness on surface residual stresses for finish hard turning of through-hardened AISI 52100 steel. They showed that tool edge geometry is highly influential on surface residual stresses, which were measured using X-ray diffraction. Depending on the hardness of the workpiece continuous white layers on the workpiece surface correlate with compressive residual stresses, while over-tempered regions correlate with tensile or compressive residual stresses. Liu and Guo [53] developed a thermo-elastic-viscoplastic model using explicit finite element code, Abaqus to investigate the effect of sequential cuts and tool-chip friction on residual stresses. M'Saoubi et al. [54] investigated the residual stresses induced by orthogonal cutting in AISI 316L steels. X-Ray diffraction technique was used for determining the depth profiles of the residual stresses. The effect of cutting conditions and tool properties on residual stresses was analyzed. Jacabus et al. [55] investigated machining induced residual stresses resulted from oblique machining of annealed AISI 4340. Based on the experiments performed, a plane strain thermo elastoplastic model of metal flow under flank of a cutting tool was developed. The model results demonstrated the significance of thermal and mechanical mechanisms in the development of machining induced residual stresses with thermal effects resulting in increases in the tensile character of the machining induced residual stresses. Shet and Deng [56] developed a finite element method to simulate and analyze the orthogonal metal cutting process under plane strain conditions. They focused on the residual stresses and strain fields in the finished workpiece and found that thermal cooling increases the residual stress level and the effects of the friction coefficient and rake angle to the residual stress level are nonlinear.

Currently, adequate and detailed mathematical models for the mechanics and thermal aspects of the hard turning process in the literature are mostly missing. More detailed analysis, better understanding and knowledge on forces, stresses and temperature fields, temperature gradients created during the machining and residual stresses are very critical for effective and efficient implementations of the hard turning processes.

# Chapter 3

# CUTTER/WORKPIECE GEOMETRY AND CUTTING FORCE MODEL

## 3.1 Introduction

In this chapter, a brief introduction to turning process is given for making the reader more familiar with the definitions used in hard turning process. Differential chip loads and differential cutting force models are presented for the hard turning processes. Shear flow stress, shear and friction angles are determined from the orthogonal calibration tests and the cutting coefficients are determined from the orthogonal to oblique transformations. In order to obtain the cutting forces in the radial, tangential and feed directions, differential cutting forces are integrated over the tool workpiece engagement domain. The predicted cutting forces in three orthogonal directions are compared with the experimentally obtained ones for validation purposes. The proposed mechanical approach is summarized in Figure 3.1.

## 3.2 Summary of Turning Process

The common turning operation carried out on lathes is one of the most popular and basic practical machining operation used for producing cylindrical components. An illustrative turning process set up is shown in Figure 3.2. In Computer Numerical Control (CNC) lathes, the spindle speed and feedrate are directly programmed within the Numerical Control (NC) programs. A typical CNC lathe is shown in Figure 3.3. For the basic turning operations, feed is much smaller than the depth of cut and the depth of cut is much smaller than the workpiece diameter. The angle of inclination $i$ at the major cutting edge of the tool can be used to identify the turning process as orthogonal turning for $i = 0$, or oblique turning when $i \neq 0$ (Figure 3.4). A standard turning tool geometry is shown in Figure 3.5.

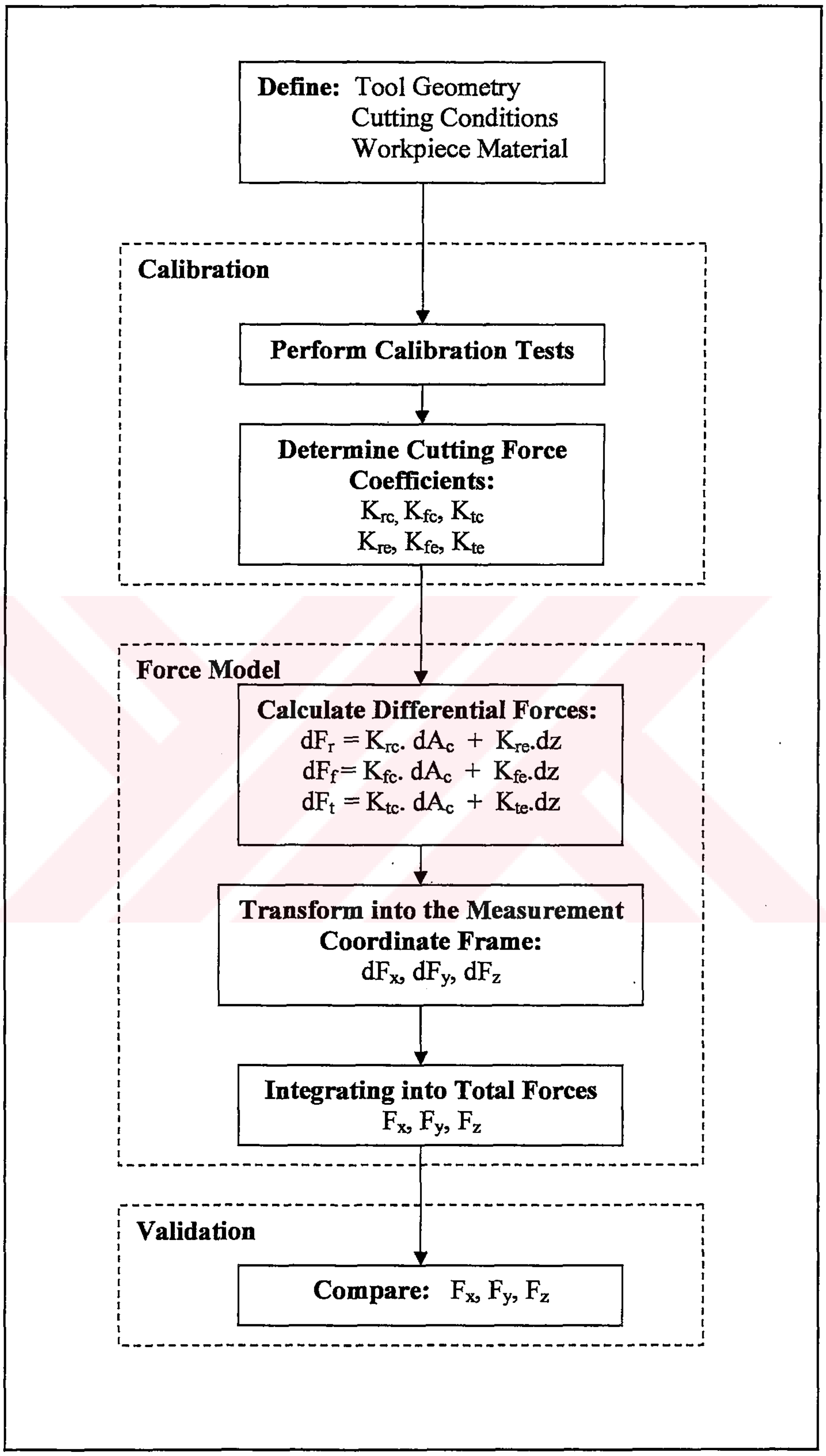


Figure 3.1: A summary chart of the proposed mechanistic approach.

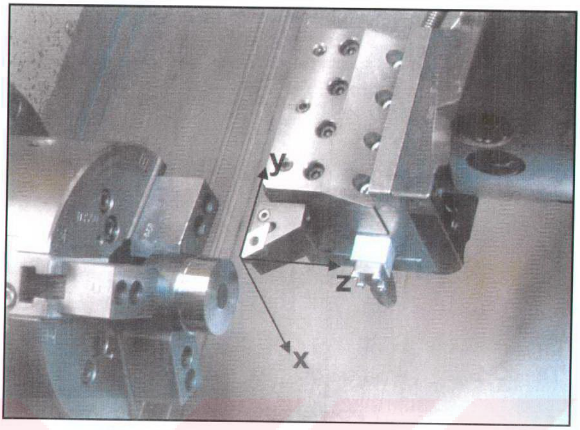


Figure 3.2: An illustrative turning process set up.

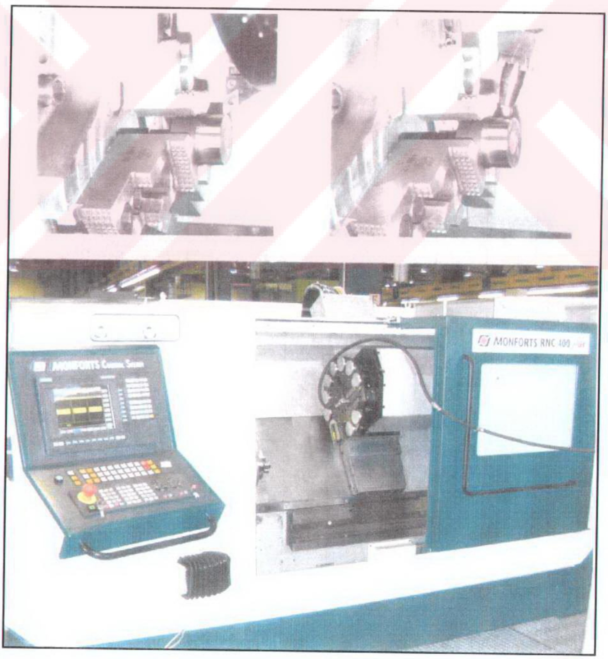


Figure 3.3: CNC turning center.

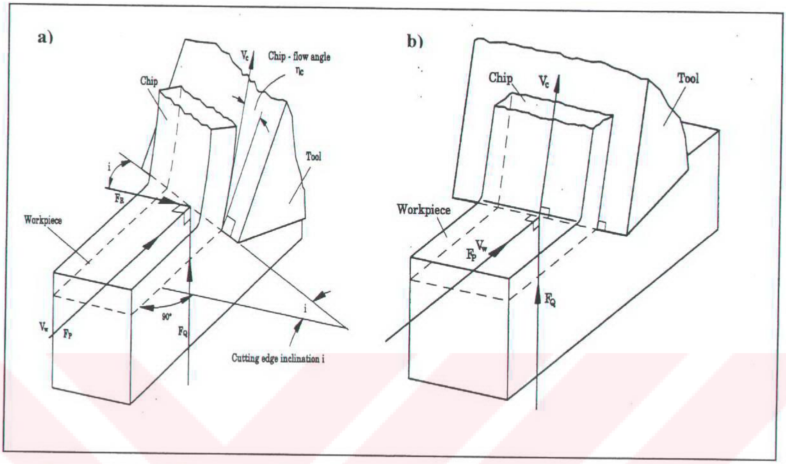


Figure 3.4 a) Oblique turning, b) Orthogonal turning, adopted from Armarego [58].

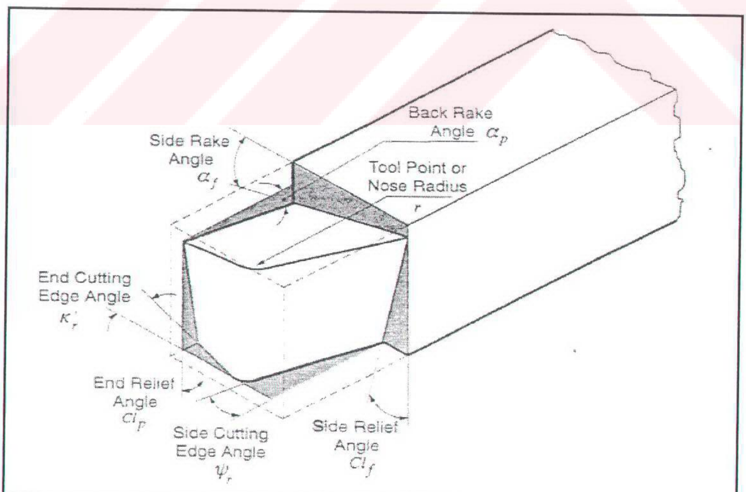


Figure 3.5: Geometry of turning tool, adopted from Altintas [57].

### 3.3 Differential Chip Loads

The chip load at any instant of time is discretized into very small elements so that at each of these discrete elements corresponding differential forces in three orthogonal directions can be computed, and integrated over the tool workpiece engagement domain to determine the total cutting forces. For this purpose, the chip load was discretized into small elements with $d\theta$ angular increments in the engagement domain (Figure 3.6). The depths of cut in hard turning are smaller than the soft turning, and they are less than nose radii of the inserts used. Therefore, the engagement domain between the workpiece and insert has two distinct regions, namely Region I and Region II (Figure 3.6), for the calculations of the local chip thicknesses and local chip loads for each discrete element.

The local chip thicknesses and chip loads are calculated for Region I ($\theta_0<\theta<\theta_1$) and Region II ($\theta_1<\theta<\theta_2$) as follows,

$$
\begin{aligned}
h_{1(\theta)} &= R - \frac{R-a}{\sin(\theta)} && \text{for } \theta_0 \le \theta \le \theta_1 \\
h_{2(\theta)} &= R - \sqrt{c^2 + R^2 - 2cR\cos(\gamma)} && \text{for } \theta_1 \le \theta \le \theta_2
\end{aligned}
\tag{3.1}
$$

where

$$
\theta_0 = \sin^{-1}(1-\frac{a}{R}), \quad \theta_1 = \frac{\pi}{2} - \tan^{-1}(\frac{R.\cos(\theta_0)-c}{R-a}),
$$
$$
\theta_2 = \frac{\pi}{2} + \sin^{-1}(\frac{c}{2R}), \quad \gamma = \theta - \sin^{-1}(\frac{c}{R}\sin(\pi-\theta))
$$

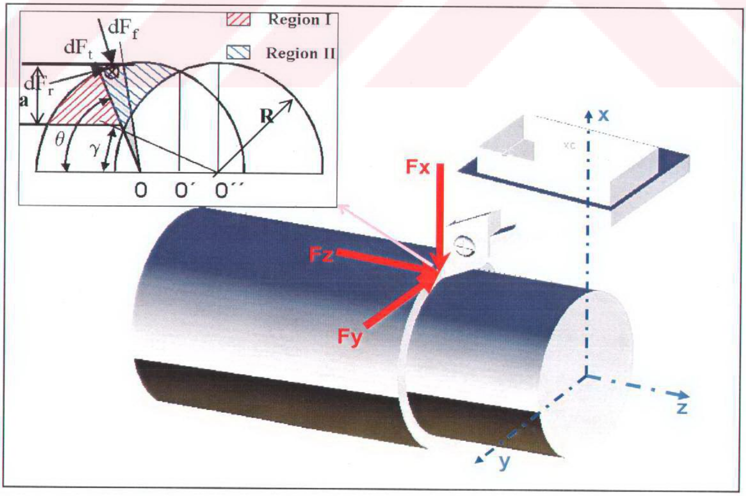


Figure 3.6: Illustration of the chip load and differential cutting forces in hard turning process.

Differential chip load for each discrete element can be determined as the following,

$$dA = h.ds = h.R.d\theta \tag{3.2}$$

where $h$ takes the values of $h_1$ or $h_2$ depending whether the respective discrete element is located in Region I or II, respectively.

### 3.4 Differential Cutting Forces

The forces acting during the cutting are composed of two main force components, namely cutting force components due to the shearing mechanism and edge force components mainly due to plowing mechanism. The discrete cutting force components are proportional to local chip load by local oblique cutting force coefficients. The discrete edge force components are proportional to length of local chip-insert contact with an edge force coefficient. In order to predict the total cutting forces, local cutting force coefficient, and subsequently, differential cutting forces are needed to be determined for each discrete chip element [57].

Orthogonal to oblique transformation technique is used to determine the oblique cutting coefficients. In this technique, shear flow stress, shear and friction angles are determined from the orthogonal calibration tests for the workpiece material and tool combinations. Later, using the values of shear flow stress, shear and friction angles, the cutting force coefficients for the oblique cutting are obtained from the orthogonal to oblique transformations [57].

The tangential, radial and feed components of cutting force for each discrete element can be written in terms of cutting and edge forces as follows,

$$\begin{aligned} dF_{t(\theta)} &= K_{tc(\theta)}.dA_{(\theta)} + K_{te}.ds \\ dF_{r(\theta)} &= K_{rc(\theta)}.dA_{(\theta)} + K_{re}.ds \\ dF_{f(\theta)} &= K_{fc(\theta)}.dA_{(\theta)} + K_{fe}.ds \end{aligned} \tag{3.3}$$

in the above equation $K_{tc(\theta)}, K_{rc(\theta)}, K_{fc(\theta)}$ are tangential, radial and feed cutting force coefficients, respectively, to be determined from orthogonal to oblique transformations. $dA_{(\theta)}$ and $ds$ are differential chip load and differential cutting edge length for each discrete element, respectively. Therefore, the differential force equation above can be rewritten in terms of local chip thickness of each discrete element and the insert nose radius ( $R$ ) as follows,

$$dF_{t(\theta)} = \left[K_{tc(\theta)}.h_{(\theta)} + K_{te}\right]R.d\theta$$
$$dF_{r(\theta)} = \left[K_{rc(\theta)}.h_{(\theta)} + K_{re}\right]R.d\theta \tag{3.4}$$
$$dF_{f(\theta)} = \left[K_{fc(\theta)}.h_{(\theta)} + K_{fe}\right]R.d\theta$$

It should be mentioned that in Region I, $h_{1(\theta)}$ values, and in Region II, $h_{2(\theta)}$ values are used in the above differential cutting force computations. The tangential, radial and feed cutting force coefficients are determined from the following equations [57],

$$K_{tc(\theta)} = \frac{\tau_s}{\sin(\phi_n)} \frac{\cos(\beta_n - \alpha_n) + \tan(i).\tan(\eta).\sin(\beta_n)}{\sqrt{\cos^2(\phi_n + \beta_n - \alpha_n) + \tan^2(\eta)\sin^2(\beta)}}$$
$$K_{rc(\theta)} = \frac{\tau_s}{\sin(\phi_n)} \frac{\cos(\beta_n - \alpha_n).\tan(i) - \tan(\eta).\sin(\beta_n)}{\sqrt{\cos^2(\phi_n + \beta_n - \alpha_n) + \tan^2(\eta)\sin^2(\beta)}} \tag{3.5}$$
$$K_{fc(\theta)} = \frac{\tau_s}{\sin(\phi_n).\cos(i)} \frac{\sin(\beta_n - \alpha_n)}{\sqrt{\cos^2(\phi_n + \beta_n - \alpha_n) + \tan^2(\eta)\sin^2(\beta)}}$$

In these equations, $\tau_s, \phi_n$ and $\beta_n$ are, shear flow stress, shear and friction angles determined from the orthogonal calibration tests, respectively. $\eta$ is the chip flow angle that is determined from Stabler's rule (i.e., $\eta = i$). $i$ is the local inclination angle of discrete cutting edge which can be determined from,

$$i = \tan^{-1}(\tan(\alpha_p).\cos(\psi_r) + \tan(\alpha_f).\sin(\psi_r)) \tag{3.6}$$

where $\alpha_p$ and $\alpha_f$ are the back rake and side rake angles of the tool. $\psi_r$ is the side cutting edge angle and is equal to rotational position of the respective discrete element (i.e., for each discrete element, $\psi_r = \theta$ ).

Normal rake angle ( $\alpha_n$ ) can be determined from

$$\alpha_n = \tan^{-1}(\tan(\alpha_0).\cos(i)) \tag{3.7}$$

where orthogonal rake angle ( $\alpha_0$ ) is,

$$\alpha_0 = \tan^{-1}(\tan(\alpha_f).\cos(\psi_r) + \tan(\alpha_p).\sin(\psi_r)) \tag{3.8}$$

The edge forces are generated not due to the cutting mechanism but the plowing mechanism. Therefore, the edge coefficients ( $K_{te}$ and $K_{fe}$ ) can be easily determined by extending the feedrate-force graphs obtained from the orthogonal cutting calibration tests to the zero feedrate. In the orthogonal calibration tests, $K_{re}$ is assumed to be zero since nearly no radial force should exist in these tests.

Differential tangential, radial and feed forces can be transformed to the Cartesian force measurement coordinate system, in three orthogonal directions (i.e., X,Y, and Z), as follows,

$$\begin{aligned} dF_x &= dF_t \\ dF_y &= dF_f.\sin(\theta) - dF_r.\cos(\theta) \\ dF_z &= dF_f.\cos(\theta) + dF_r.\sin(\theta) \end{aligned} \tag{3.9}$$

Total force components acting during the machining can be determined by integrating the discrete force values, $F_x$, $F_y$, and $F_z$ (tangential, radial, feed cutting force components respectively), acting on each differential chip load:

$$F_X = \sum_{i=1}^{N} dF_X,\ F_Y = \sum_{i=1}^{N} dF_Y,\ F_Z = \sum_{i=1}^{N} dF_Z \tag{3.10}$$

where N represents the number of the discrete elements.

The total cutting torque ($T_c$) and power ($P_c$) drawn from the spindle drive are,

$$\begin{aligned} T_c &= \frac{D}{2}.F_t \\ P_c &= V.F_t \end{aligned} \tag{3.11}$$

where D is the diameter of the turned shaft, $V = \pi.D.n$ is the cutting speed and n (rev/sec) is the spindle revolution.

### 3.5 Calibration Process

In order to determine the cutting force coefficients of the model, orthogonal calibration tests were performed on the commonly used automobile transmission material of induction hardened 51CrV4. The hardness of material was 68 HRC. The cutting tests were made in a Monfort 400 RNC Plus CNC turning machine under rigid cutting conditions at the WZL, Technical University Aachen, Germany. The cutting inserts used in the calibrations were Seco CBN 100 with the chamfer angles of -14° and -25°. The experimental set up is shown in Figure 3.7. The hardness plot of the 51CrV4 is shown in Figure 3.8.

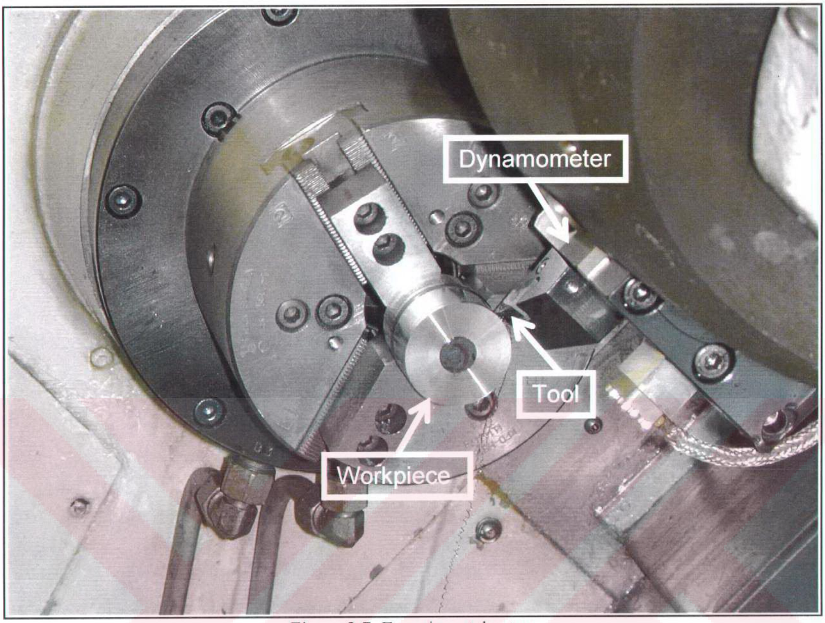


Figure 3.7: Experimental setup

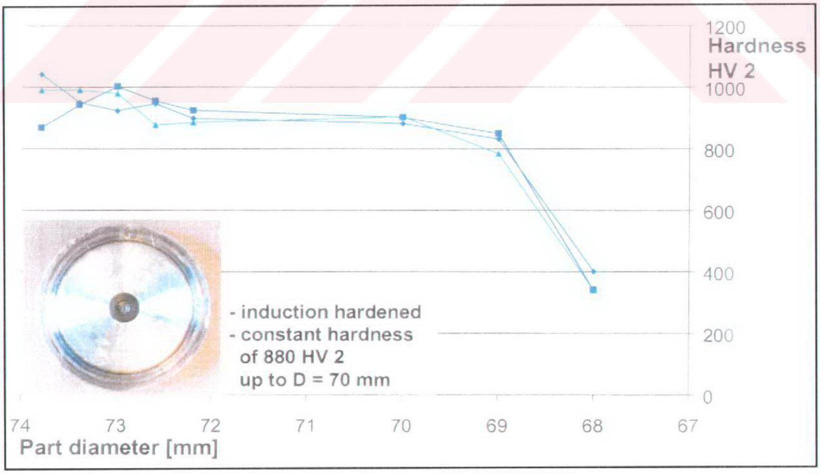


Figure 3.8: Hardness plot of workpiece material, Induction Hardened 51 CrV4.

The cutting forces are sensed by the piezoelectric transducer in the dynamometer and an electric charge output is the outcome of this process. This electric charge is later taken by the charge amplifier and converted into voltage output. Subsequently, through use of a proper data acquisition card and software, the voltage output is displayed and recorded as cutting forces in unit of Newton. The detailed illustration of the experimental setup is shown in Figure 3.9. Displaying and recording of the measured data were realized with a data acquisition program, LabVIEW (See Figure 3.10 for a sample output screen of LabVIEW).

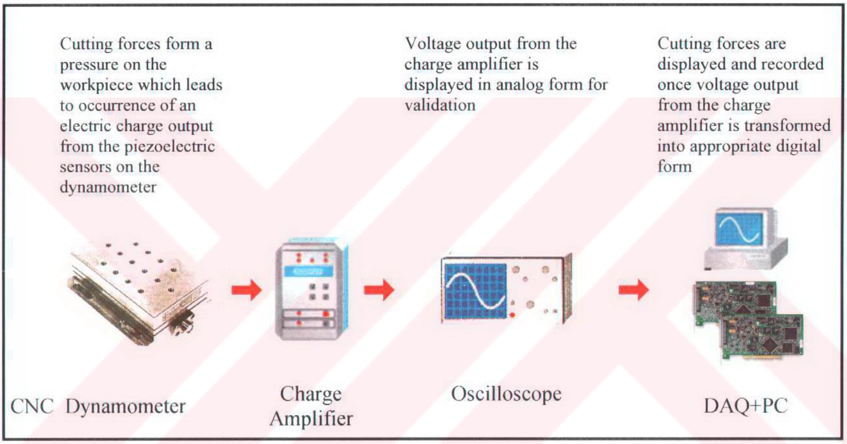


Figure 3.9: The detailed illustration of experimental setup.

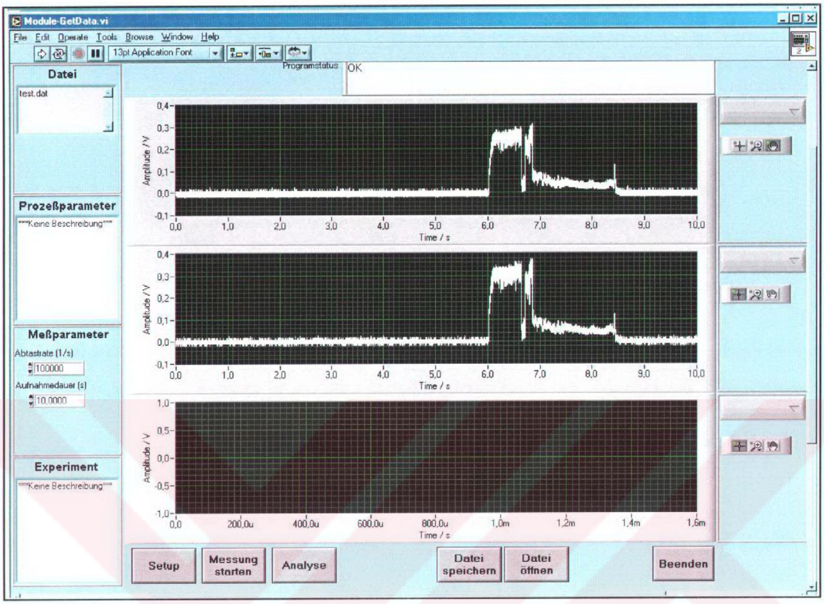


Figure 3.10: Sample output screen of LabVIEW.

In the calibration tests without chipping, the lower and upper limits of the cutting speeds were 90 and 140 [m/min]. The feedrate values were changed between 0.01 and 0.08 [mm/rev] with 0.01 [mm/rev] increments. Cutting force components were collected in two orthogonal directions (i.e., tangential and feed directions) at the sampling rate of 6000 [Hz] in order to determine the average friction angle, the shear flow stress and the edge force coefficients. Shear angle value was determined from the chip ratios by using the formulation below:

$$\phi_c = \tan^{-1}\frac{r_c.\cos\alpha_r}{1 - r_c.\sin\alpha_r} \tag{3.12}$$

where $\phi_c$ is the shear angle, $r_c = h/h_c$, $h$ is the uncut chip thickness, $h_c$ is the deformed chip thickness and $\alpha_r$ is the rake angle. The calculation of average shear angle is shown in Table 3.1.

Table 3.1 Calculation of shear angle

| Rake Angle [deg] | Cutting Speed v [m/min] | Feed Rate f [mm] | Mass [g] | Chip Length [mm] | Chip Thickness [mm] | Chip Ratio h/hc | Rake Angle [rad] | Shear Angle [rad] | Shear Angle [°] |
|---|---|---|---|---|---|---|---|---|---|
| -14 | 90 | 0.01 | 0.003 | 9.21 | 0.021 | 0.479 | -0.244 | 0.395 | 22.609 |
| -14 | 90 | 0.02 | 0.004 | 8.19 | 0.032 | 0.623 | -0.244 | 0.484 | 27.722 |
| -14 | 90 | 0.03 | 0.005 | 8.94 | 0.035 | 0.854 | -0.244 | 0.602 | 34.476 |
| -14 | 90 | 0.05 | 0.008 | 10.19 | 0.047 | 1.060 | -0.244 | 0.686 | 39.299 |
| -14 | 90 | | | | | | | | |
| -14 | 90 | **Force signals could not be acquired because of micro chipping of the tool** | | | | | | | |
| -14 | 90 | | | | | | | | |
| -14 | 140 | 0.01 | 0.003 | 12.16 | 0.015 | 0.654 | -0.244 | 0.501 | 28.722 |
| -14 | 140 | 0.02 | 0.005 | 20.00 | 0.016 | 1.248 | -0.244 | 0.749 | 42.926 |
| -14 | 140 | 0.03 | 0.005 | 11.18 | 0.029 | 1.046 | -0.244 | 0.681 | 39.016 |
| -14 | 140 | 0.05 | 0.005 | 10 | 0.033 | 1.529 | -0.244 | 0.825 | 47.287 |
| -14 | 140 | | | | | | | | |
| -14 | 140 | **Force signals could not be acquired because of micro chipping of the tool** | | | | | | | |
| -14 | 140 | | | | | | | | |
| | | | | | | | | | 35.257 |
| -25 | 90 | 0.01 | 0.003 | 10.77 | 0.018 | 0.542 | -0.436 | 0.380 | 21.784 |
| -25 | 90 | 0.02 | 0.005 | 13.10 | 0.025 | 0.801 | -0.436 | 0.497 | 28.483 |
| -25 | 90 | 0.03 | 0.004 | 10.83 | 0.025 | 1.207 | -0.436 | 0.627 | 35.916 |
| -25 | 90 | 0.05 | 0.008 | 13.47 | 0.037 | 1.347 | -0.436 | 0.661 | 37.881 |
| -25 | 90 | 0.06 | 0.015 | 19.7 | 0.048 | 1.246 | -0.436 | 0.637 | 36.490 |
| -25 | 90 | 0.07 | 0.011 | 14.48 | 0.046 | 1.506 | -0.436 | 0.695 | 39.829 |
| -25 | 90 | 0.08 | 0.011 | 16.06 | 0.044 | 1.806 | -0.436 | 0.748 | 42.867 |
| -25 | 140 | 0.01 | 0.004 | 9.49 | 0.024 | 0.423 | -0.436 | 0.314 | 18.015 |
| -25 | 140 | 0.02 | 0.003 | 6.50 | 0.030 | 0.676 | -0.436 | 0.445 | 25.479 |
| -25 | 140 | 0.03 | 0.005 | 16.43 | 0.020 | 1.508 | -0.436 | 0.696 | 39.849 |
| -25 | 140 | 0.05 | 0.009 | 15.68 | 0.036 | 1.374 | -0.436 | 0.667 | 38.234 |
| -25 | 140 | 0.06 | 0.013 | 22.53 | 0.037 | 1.622 | -0.436 | 0.717 | 41.096 |
| -25 | 140 | 0.07 | 0.006 | 9.95 | 0.039 | 1.811 | -0.436 | 0.749 | 42.914 |
| -25 | 140 | 0.08 | 0.008 | 15.69 | 0.031 | 2.611 | -0.436 | 0.844 | 48.365 |
| | | | | | | | | **Average Shear Angle =35.51** | |

The force outputs of the system for various feedrate and cutting speed values are illustrated in Figures 3.11-14. Typical variations of the cutting force components in the tangential and feed directions for various feedrates are shown in Figures 3.15-18.

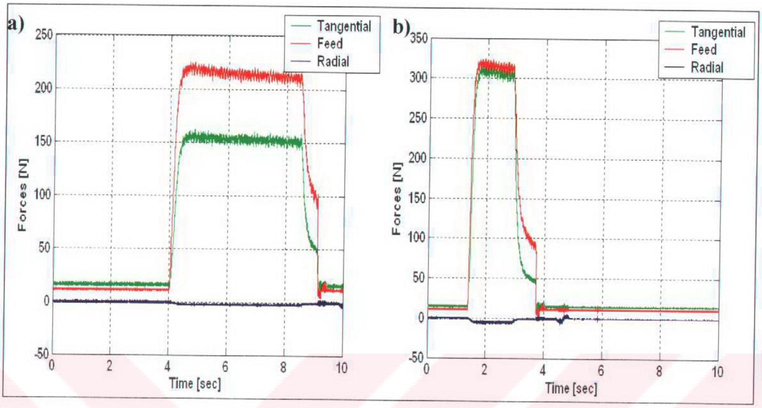


Figure 3.11: Illustration of the measured cutting force values for the the cutting speed of 140 [m/min], with the insert of -25 ° rake angle and for the feedrate of a) 0.01 [mm/rev], b) 0.03 [mm/rev].

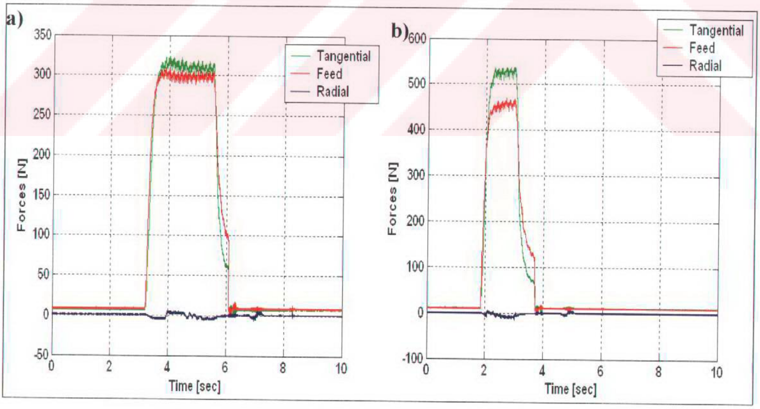


Figure 3.12: Illustration of the measured cutting force values for the cutting speed of 90 [m/min], with the insert of -25 ° rake angle and for the feedrate of a) 0.03 [mm/rev], b) 0.06 [mm/rev].

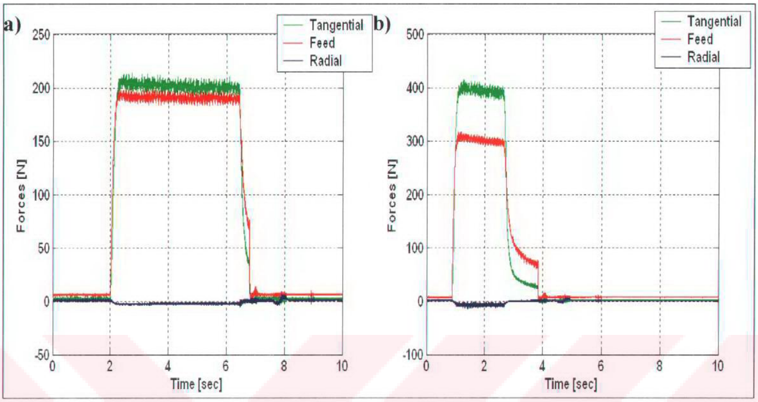


Figure 3.13: Illustration of the measured cutting force values for the cutting speed of 140 [m/min], with the insert of -14° rake angle and for the feedrate of a) 0.02 [mm/rev], b) 0.05 [mm/rev]

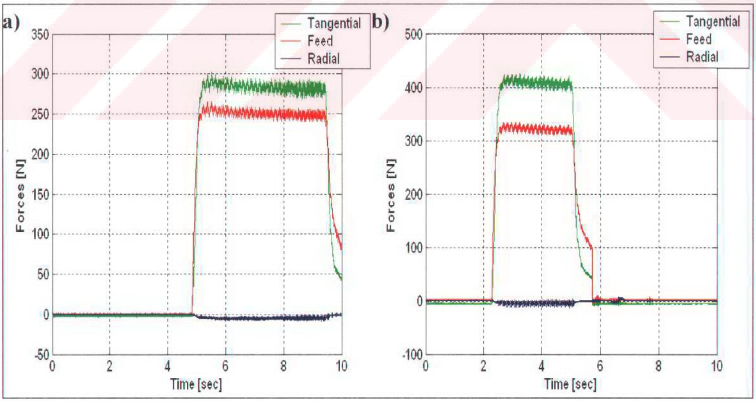


Figure 3.14: Illustration of the measured cutting force values for the cutting speed of 90 [m/min], with the insert of -14° rake angle and for the feedrate of a) 0.03 [mm/rev], b) 0.05 [mm/rev]

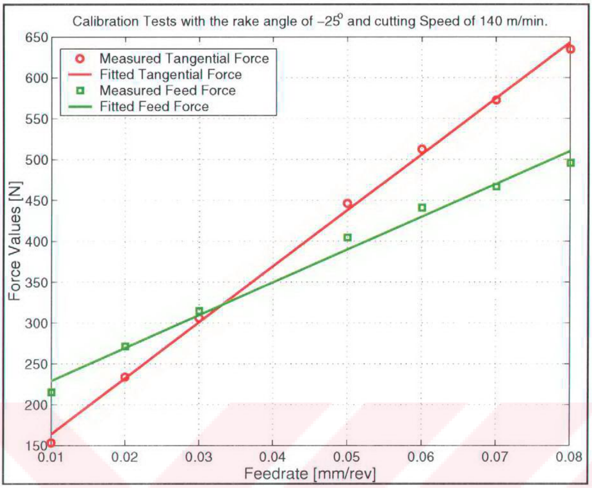


Figure 3.15: Measured cutting force values during the machining of 51CrV6 at the speed of 140 [m/min] with the insert of -25° rake angle.

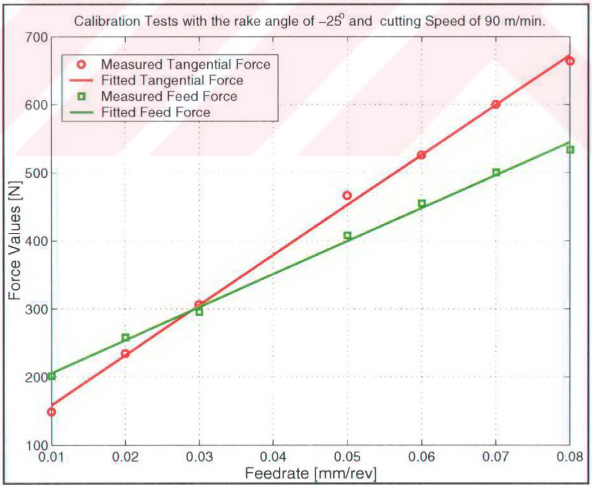


Figure 3.16: Measured cutting force values during the machining of 51CrV6 at the speed of 90 [m/min] with the insert of -25° rake angle.

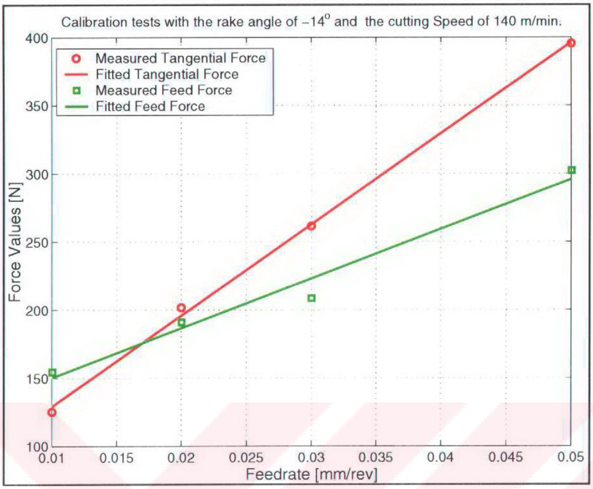


Figure 3.17: Measured cutting force values during the machining of 51CrV6 at the speed of 140 [m/min] with the insert of -14° rake angle.

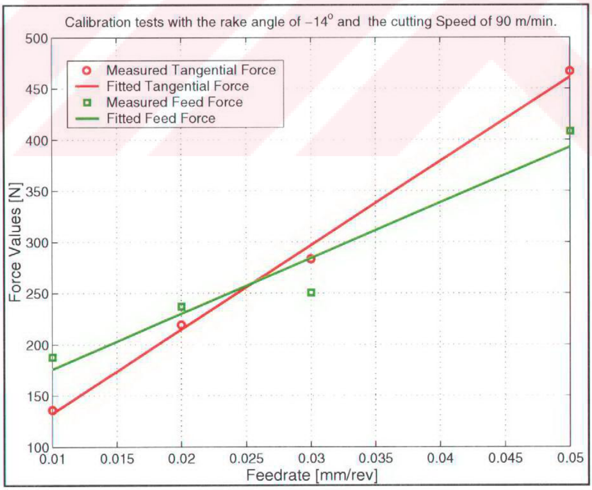


Figure 3.18: Measured cutting force values during the machining of 51CrV6 at the speed of 90 [m/min] with the insert of -14° rake angle.

The determination of cutting and edge force coefficients from the experimental force data is summarized in Figure 3.19. From the orthogonal calibration tests, the values in Table 3.2 were obtained.

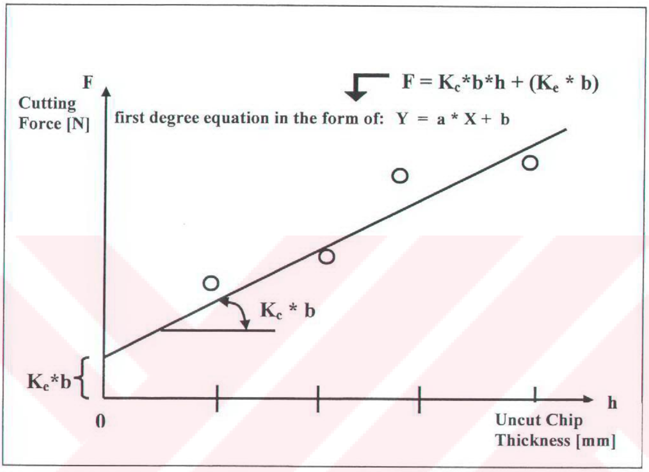


Figure 3.19: Determination of cutting coefficients

Table 3.2: Orthogonal test results

| | |
|---|---|
| Shear angle ($\phi_n$) | 35.5° |
| Average friction angle ($\beta_n$) | 12° |
| Average shear flow stres ($\tau_s$) | 973 [MPa] |
| Tangential force edge coefficient ($K_{te}$) | 36.52 [N/mm] |
| Feed force edge coefficient ($K_{fe}$) | 72.76 [N/mm] |

### 3.6 Validation Tests

After obtaining these values from the orthogonal calibration tests, simulations were run for various cutting conditions. In the validation tests, the cutting speeds and radial depths of cut were set at the values of 90, 120, 140 [m/min] and 60, 80, 100, 120 [$\mu$], respectively. Seco CBN 10 with the insert radius of 0.8 [mm] was utilized. The geometry of the insert was analyzed in a microscope and is shown in Figure 3.20. The chamfer angle of the insert was -20°. With the tool holder (Seco CTGPL 1616--11), the effective rake angle on the chamfered part of the insert became -26° and the side rake angle was 0°. The length of the chamfer was 150 [μ]. Considering the radial depths of cut given above, it should be noted that all the experimental validations were performed in the chamfered region of the insert. A typical set of measured cutting force data sampled at 6000 [Hz] is shown in Figure 3.21 for the radial depth of cut of 60 [μ], the cutting speed of 90 [m/min], and feedrate of 0.12 [mm/rev]. The validation results are shown in Figures 3.22-27 for the various cutting speeds and radial depth of cut values.

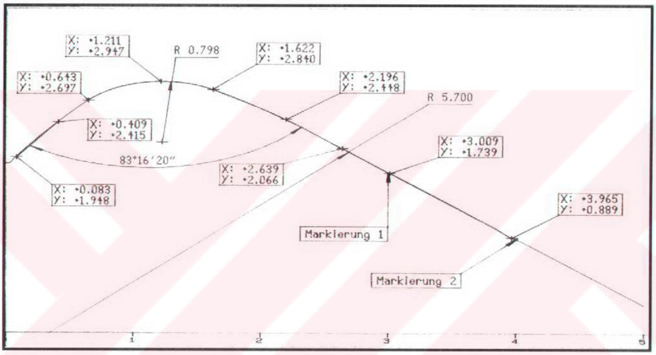


Figure 3.20: Insert geometry of Seco DNGA 150608 S-L1 CBN 10 used in the validation tests.

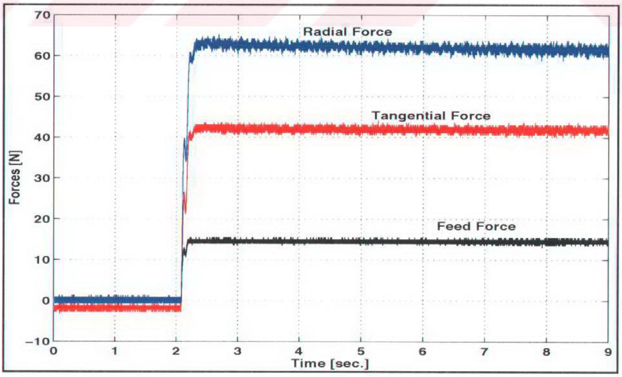


Figure 3.21: Illustration of the measured cutting force values for the depth of cut of 60 [μ], the cutting speed of 90 [m/min] and for the feedrate of 0.12 [mm/rev].

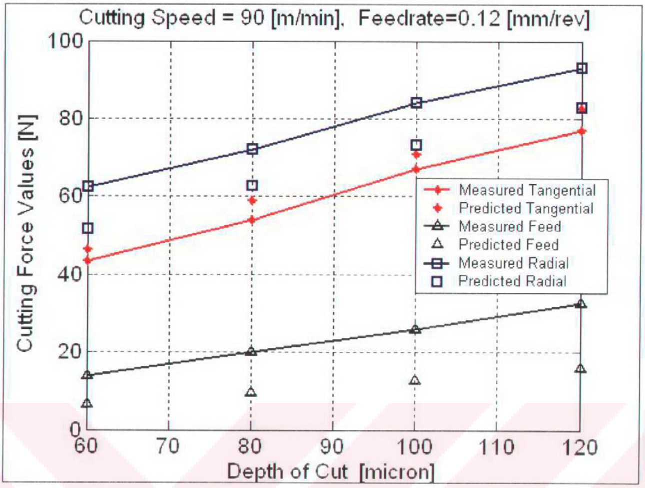


Figure 3.22: Comparison of the tangential, feed and radial components of the experimentally measured and simulated cutting forces for the cutting speed of 90 [m/min], and feedrate of 0.12 [mm/rev].

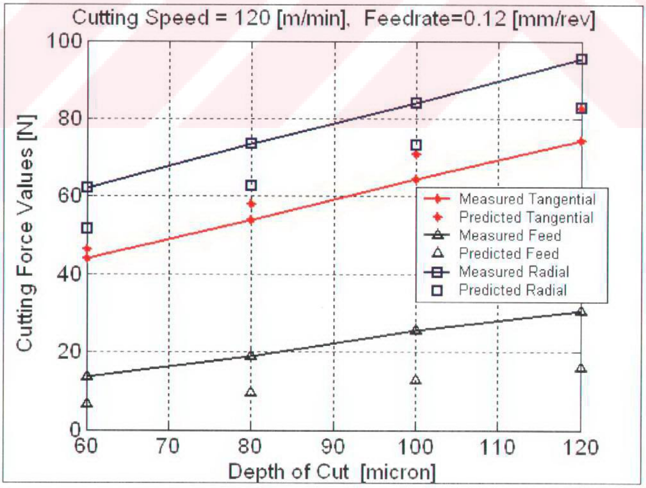


Figure 3.23: Comparison of the tangential, feed and radial components of the experimentally measured and simulated cutting forces for the cutting speed of 120 [m/min], and feedrate of 0.12 [mm/rev].

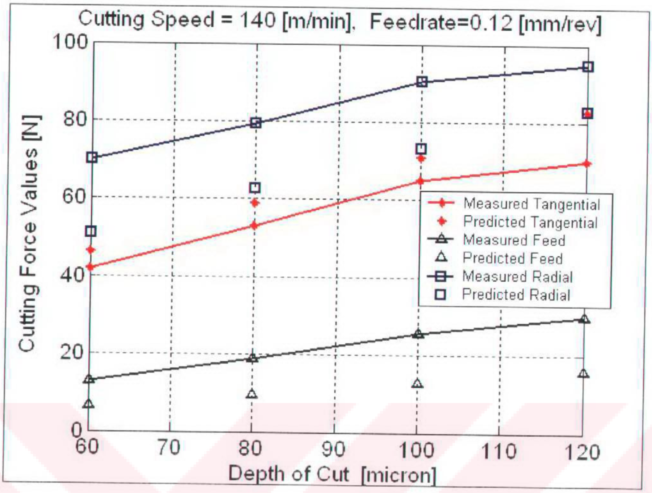


Figure 3.24: Comparison of the tangential, feed and radial components of the experimentally measured and simulated cutting forces for the cutting speed of 140 [m/min], and feedrate of 0.12 [mm/rev].

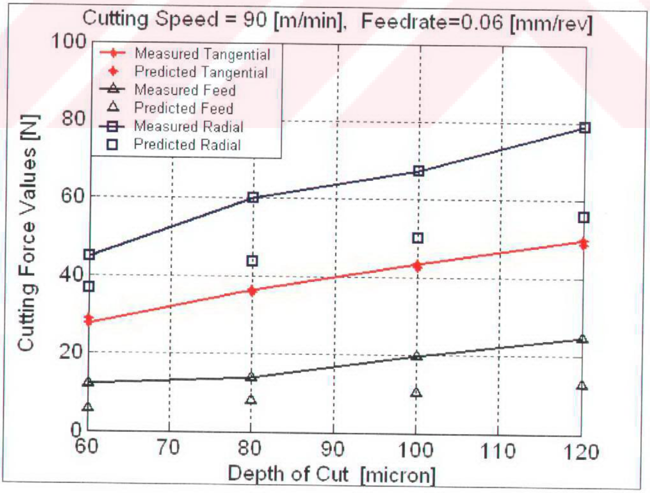


Figure 3.25: Comparison of the tangential, feed and radial components of the experimentally measured and simulated cutting forces for the cutting speed of 90 [m/min], and feedrate of 0.06 [mm/rev].

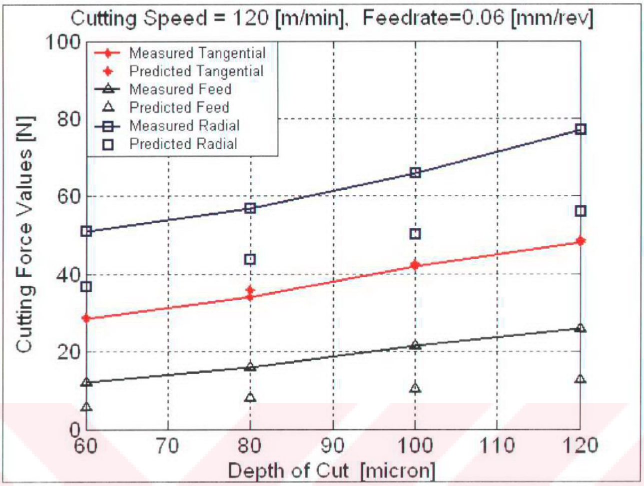


Figure 3.26: Comparison of the tangential, feed and radial components of the experimentally measured and simulated cutting forces for the cutting speed of 120 [m/min], and feedrate of 0.06 [mm/rev].

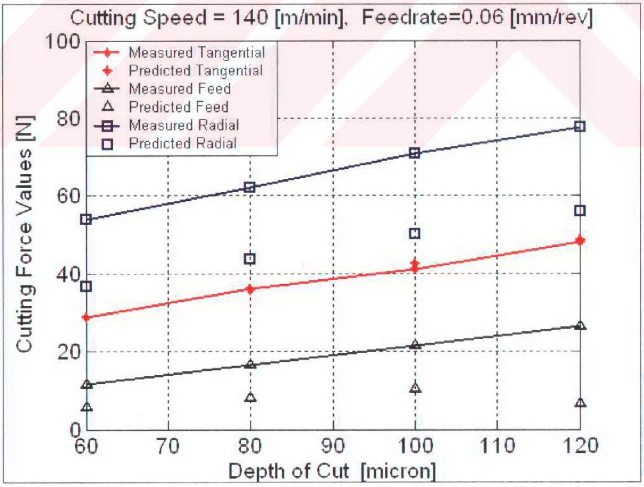


Figure 3.27: Comparison of the tangential, feed and radial components of the experimentally measured and simulated cutting forces for the cutting speed of 140 [m/min], and feedrate of 0.06 [mm/rev].

In Figures 3.28 and 3.29 the force data is simulated for the chamfer angle of -26°, side rake angle of 0° and the feedrate of 0.12 and 0.06 [mm/rev], respectively. It is observed that the tangential cutting force predictions are matching well with the experimental measured values in all the cutting conditions. Overall, components of radial and feed force predictions agree well with the trends of the measured cutting forces with small magnitude discrepancies. The small differences in magnitudes may be due to the fact that in the model based predictions only the average friction value was used, and ploughing forces were assumed to be negligible.

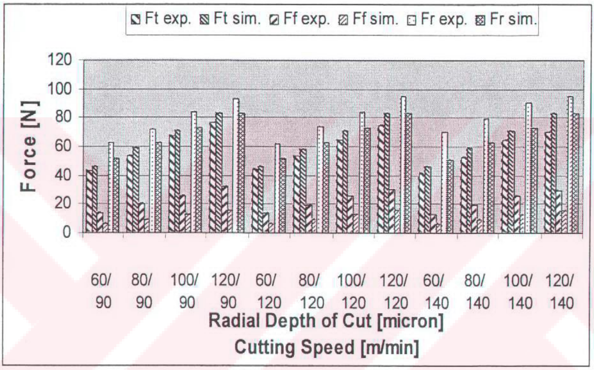


Figure 3.28: Comparison of the tangential, feed and radial components of the experimentally measured and simulated cutting forces for the feedrate of 0.12 mm/rev.

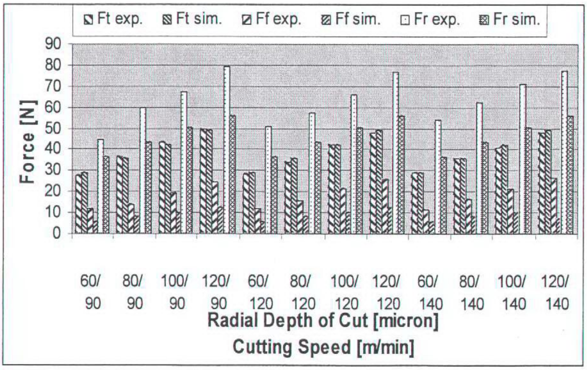


Figure 3.29: Comparison of the tangential, feed and radial components of the experimentally measured and simulated cutting forces for the feedrate of 0.06 mm/rev.

# Chapter 4

# DYNAMIC MODELING OF THE WORKPIECE AND MACHINE TOOL

## 4.1 Introduction

The development of a turning process model which is capable of predicting the dynamic cutting forces, tool and workpiece deflections, and surface errors will enable more efficient selection of cutting process parameters, such as feed, cutting speed, and cutting tool geometry. This research develops a process model for prediction of dynamic cutting forces and surface errors in hard turning. In addition, the research also focuses on analyzing the combined effects of tool geometry and machining conditions on the process performance for more efficient and reliable process planning. A generalized dynamic model for the turning process is formulated by adding the effects of dynamic deflections in the cutting tool, on the chip thickness and depth of cut. Using the dynamic chip thickness and depth of cut, dynamic chip load is calculated which is used to predict the dynamic forces.

## 4.2 Dynamic Process Simulation Model

Dynamic system model utilized for the hard turning simulation is illustrated in Figure 4.1. The input parameters of the dynamic process simulation model are the cutting speed, feedrate, depth of cut, the diameter of the workpiece, and modal parameters. The modal parameters were measured experimentally from the Frequency Response Functions of the system. The other input parameters are determined by the user. Using the experimentally measured modal parameters, the transfer function of the system is determined. The cutting forces are multiplied by the transfer function and the instantaneous vibration values in both radial and feed directions are determined. These vibration values affect the current tool position which consequently changes the dynamic chip load. Using the new chip load, cutting forces are calculated and this process is repeated for each time step. Therefore, tangential, radial, and feed forces are calculated at each time step.

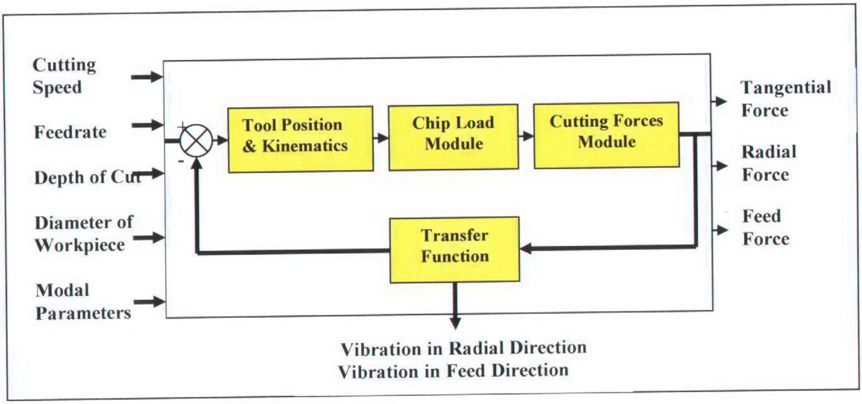


Figure 4.1: Dynamic system module.

### 4.3 Identification of Structural Dynamic Parameters

Modal parameters of the system must be known in order to obtain instantaneous chip thickness which is changing under the effect of vibrations generated. Therefore, using Frequency Response Functions (FRF), stiffness, damping ratio, natural frequency and residues of the system can be obtained.

The FRF describes how a system vibrates in response to different frequencies of excitation. The FRF is a measurable function, and it can be used to compare and predict the performance of cutters and machine tools. Whereas single degree of freedom systems have one natural frequency, multiple degree of freedom systems have one natural frequency for each degree of freedom. Each natural frequency has a corresponding characteristic deformation pattern (mode shape). Vibration in multiple degree of freedom systems may be considered as a sum of vibrations in the individual modes.

A FRF can be further evaluated as real and imaginary parts, as shown in Figure 4.2. The equations that lead to the generation of the real and imaginary graphs are also identified. The real part of the FRF is used to calculate damping and the imaginary part is used to calculate stiffness of the system.

Using the FRFs of the system in radial and feed directions, modal parameters, $\omega_n$, $\zeta$ and k are evaluated for each mode as shown in the Figure 4.2.

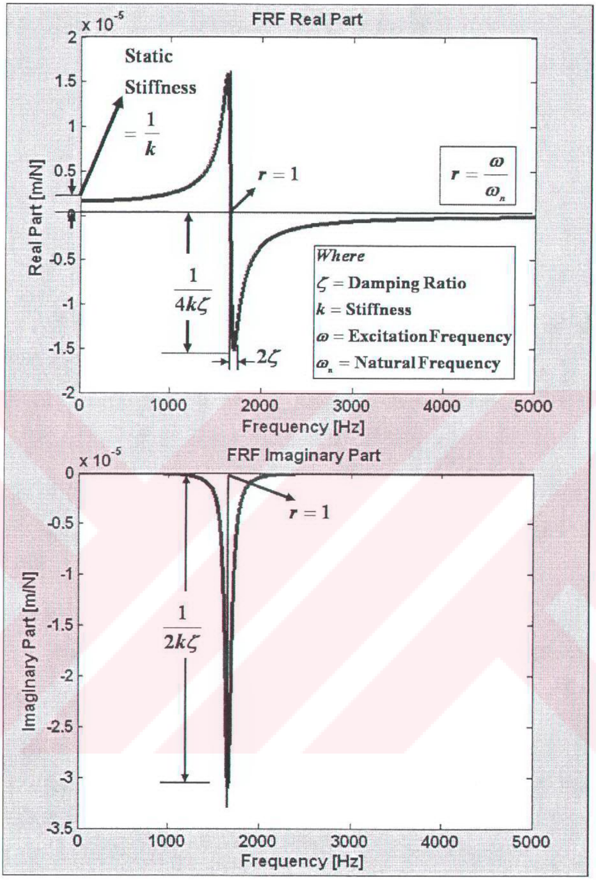


Figure 4.2: Real and imaginary parts of FRF.

### 4.4 Transfer Functions of the Structure

A simple structure with a single degree of freedom system can be modeled by a combination of mass $[M]$, spring $[K]$, and damping $[C]$ elements. When an external force $F(t)$ is exerted on the structure, its governing equation of motion is described by the following differential equations in time, and Laplace domains.

In Time Domain:

$$[M]\ddot{x}(t)+[C]\dot{x}(t)+[K]x(t)=F(t) \tag{4.1}$$

In Laplace Domain:

$$s^2[M]X(s)+s[C]X(s)+[K]X(s)=F(s) \tag{4.2}$$

or,

$$h(s)=\frac{X(s)}{F(s)}=\frac{1/m}{s^2+2\zeta\omega_n s+\omega_n{}^2} \tag{4.3}$$

where $h(s)$, $\omega_n$, $k$ and $\zeta$ are the transfer function, natural frequency, modal stiffness, and damping ratio of the system respectively. $s^2+2\zeta_i\omega_{ni}s+\omega_{ni}{}^2$ is the characteristic equation of the system that has two complex conjugate roots,

$$s_1=-\zeta\omega_n+j\omega_d \quad \text{and} \quad s_1{}^*=-\zeta\omega_n-j\omega_d$$

The transfer function can be expressed by its partial fraction expansion as,

$$h(s)=\frac{r}{s-s_1}+\frac{r^*}{s-s_1{}^*}=\frac{\alpha+\beta s}{s^2+2\zeta w_n s+w_n{}^2} \tag{4.4}$$

where the residue are:

$$r=\sigma+j\upsilon \quad \text{and} \quad r^*=\sigma-j\upsilon$$

and the corresponding parameters are:

$$\alpha=2(\zeta\omega_n\sigma-\omega_d\upsilon), \qquad \beta=2\sigma.$$

The residues may have real and imaginary parts depending on the damping and the number of modes of the system. However, the residues have distinct values for a SDOF system:

$$r=\frac{1/m}{2jw_d}, \qquad r^*=-\frac{1/m}{2jw_d} \tag{4.5}$$

Hence, the real part of the residues must be zero ($\sigma = 0$ and $\beta = 0$) for SDOF systems.

In analytical methods of solving differential equations, the stiffness mass and damping matrices are estimated from material properties, measured forces, and responses. The modal parameters of N modes are then found by the solution of the classic eigenvector problem, and the differential equation is solved in modal coordinates. The alternative approach is to directly fit modal parameters of N modes to the experimental data. Therefore, using the experimental modal analysis method, transfer functions of the structure along the radial and feed directions are obtained respectively in the Laplace domain as,

$$\phi_r(s) = \frac{\Delta z(s)}{F_z(s)} = \sum_{i=1}^{N} \frac{\omega_{ni}^{2} / k_i}{s^2 + 2\zeta_i \omega_{ni} s + \omega_{ni}^{2}}$$

and (4.6)

$$\phi_f(s) = \frac{\Delta y(s)}{F_y(s)} = \sum_{i=1}^{N} \frac{\omega_{ni}^{2} / k_i}{s^2 + 2\zeta_i \omega_{ni} s + \omega_{ni}^{2}}$$

where $\Delta z$ and $\Delta y$ are the displacements in the radial and feed directions respectively. $N$ is the total number of modes in the system, $\omega_{ni}$ , $k_i$, and $\zeta_i$ are the experimentally found natural frequency, modal stiffness and damping ratio of the $i^{th}$ mode, respectively.

## 4.5 Simulating the Dynamic Response of the Cutter and Workpiece in Time Domain

### 4.5.1 Time Domain Dynamic Model

Once the modal parameters and transfer function of the tool and workpiece system are identified, the reaction of each structure to cutting forces can be simulated in the time domain.

A system may have many inputs and many outputs, and these may be interrelated in a complicated manner. In order to analyze such a system, it is essential to reduce the complexity of mathematical expressions, as well as to resort to computers for most of the tedious computations necessary in the analysis. The state space approach to system is best suited from this viewpoint.

While conventional control theory is based on the input-output relationships or transfer function, modern control theory is based on the description of system equations in terms of n first order differential equations, which may be combined into a first order vector matrix differential equation.

Many techniques are available for obtaining state-space representations of transfer-function systems. In our model state-space representation in the observable canonical form is used. Consider a system defined by

$$\overset{(n)}{y} + a_1 \overset{(n-1)}{y} + \ldots + a_{n-1}\dot{y} + a_n y = b_0 \overset{(n)}{u} + b_1 \overset{(n-1)}{u} + \ldots + b_{n-1}\dot{u} + b_n u \tag{4.7}$$

where $u$ is the input and $y$ is the output. This equation can also be written as

$$\frac{Y(s)}{U(s)} = \frac{b_0 s^n + b_1 s^{n-1} + \ldots + b_{n-1}s + b_n}{s^n + a_1 s^{n-1} + \ldots + a_{n-1}s + a_n} \tag{4.8}$$

and in observable canonical form:

$$\begin{bmatrix} \dot{x}_1 \\ \dot{x}_2 \\ \cdot \\ \cdot \\ \cdot \\ \dot{x}_n \end{bmatrix} = \begin{bmatrix} 0 & 0 & \ldots & 0 & -a_n \\ 1 & 0 & \ldots & 0 & -a_{n-1} \\ \cdot & \cdot & & \cdot & \cdot \\ \cdot & \cdot & & \cdot & \cdot \\ \cdot & \cdot & & \cdot & \cdot \\ 0 & 0 & \ldots & 1 & -a_1 \end{bmatrix} \begin{bmatrix} x_1 \\ x_2 \\ \cdot \\ \cdot \\ \cdot \\ x_n \end{bmatrix} + \begin{bmatrix} b_n - a_n b_0 \\ b_{n-1} - a_{n-1} b_0 \\ \cdot \\ \cdot \\ \cdot \\ b_1 - a_1 b_0 \end{bmatrix} u$$

$$y = \begin{bmatrix} 0 & 0 & \ldots & 0 & 1 \end{bmatrix} \begin{bmatrix} x_1 \\ x_2 \\ \cdot \\ \cdot \\ x_{n-1} \\ x_n \end{bmatrix} + b_0 u \tag{4.9}$$

If transfer function of our system in radial and feed directions is written in the form of Equation 4.9, $b_n$, $b_{n-1}$, $a_{n-1}$ and $a_n$ are found to be;

$$\begin{aligned} b_n &= \omega_{ni}^{2} / k_i \\ b_{n-1} &= 0 \\ a_{n-1} &= 2\zeta_i \omega_{ni} \\ a_n &= \omega_{ni}^{2} \end{aligned} \tag{4.10}$$

where $n$ equals to 2 for our SDOF system.

By using the Equation 4.10 the transfer function of the workpiece-cutting tool system is converted into observable state-space canonical form, in radial and feed directions respectively, for each mode as:

$$\begin{bmatrix} \dot{z}_{1i}(t) \\ \dot{z}_{2i}(t) \end{bmatrix} = \begin{bmatrix} 0 - \omega_{ni}^{2} \\ 1 - 2\zeta_i \omega_{ni} \end{bmatrix} \begin{bmatrix} z_{1i}(t) \\ z_{2i}(t) \end{bmatrix} + \begin{bmatrix} \omega_{ni}^{2} / k_i \\ 0 \end{bmatrix} F_z(t)$$
$$\Delta z(t) = z_2(t)$$

$$\begin{bmatrix} \dot{y}_{1i}(t) \\ \dot{y}_{2i}(t) \end{bmatrix} = \begin{bmatrix} 0 - \omega_{ni}^{2} \\ 1 - 2\zeta_i \omega_{ni} \end{bmatrix} \begin{bmatrix} y_{1i}(t) \\ y_{2i}(t) \end{bmatrix} + \begin{bmatrix} \omega_{ni}^{2} / k_i \\ 0 \end{bmatrix} F_y(t)$$
$$\Delta y(t) = y_2(t). \tag{4.11}$$

where $F_z$ and $F_y$ are the force inputs in feed and radial directions. $z$ and $y$ are the displacement and $\Delta z$ and $\Delta y$ are the dynamic deflection values in feed and radial directions, respectively.

The fourth order Runge-Kutta equation is used in the numerical integration of the state-space equation. The total radial and feed direction displacements of the tool are evaluated by summing the vibrations contributed by all natural modes of the system.

### 4.5.2 Runge-Kutta 4th Order Integration Algorithm

The 4th order Runge-Kutta formula is by far one of the most common and most preferred numerical integration algorithms. Consider the first part of Equation 4.9 which evaluates the derivatives of $x_1$ to $x_n$ for each point. The force $F$ in the turning process is a function of the cutting conditions, and the relative position between the cutter and the workpiece, which is a function of the position state variables $y_1$ to $y_n$ and of time, $t$. If these parameters are generalized, letting $v_i$ $(i = 1,2,3,...)$ represent the state variables for all points on the structures, the time derivative of a state $v_i$ is written as a function of time;

$$v_i = f'(t, v_1, v_2, ...) \quad i = 1, 2, 3, ... \tag{4.12}$$

The states at time step $n+1$ are evaluated based on the states at the previous time step $n$ with the following four stage set of equations:

$$
\begin{aligned}
k_{1,i} &= \Delta t.f'(t_n, v_{n,1}, v_{n,2},\ldots) \\
k_{2,i} &= \Delta t.f'(t_n + \Delta t/2, v_{n,1} + k_{1,1}/2, v_{n,2} + k_{1,2}/2,\ldots) \\
k_{3,i} &= \Delta t.f'(t_n + \Delta t/2, v_{n,1} + k_{2,1}/2, v_{n,2} + k_{2,2}/2,\ldots) \\
k_{4,i} &= \Delta t.f'(t_n + \Delta t, v_{n,1} + k_{3,1}, v_{n,2} + k_{3,2},\ldots) \\
v_{n+1,i} &= v_{n,i} + \frac{k_{1,i}}{6} + \frac{k_{2i}}{3} + \frac{k_{3,i}}{3} + \frac{k_{4,i}}{6}
\end{aligned}
\tag{4.13}
$$

where $i = 1,2,3,\ldots$ The last equation above is a weighted sum of the four stages of evaluation. It is important to note that evaluating the function $f'$ during the simulation actually requires several steps. These states must first be converted to position by summing the modes.

### 4.6 Determination of Dynamic Cutting Forces

After calculating the dynamic displacement values in radial and feed directions by using the 4 th order Runge Kutta algorithm, dynamic cutting forces can be calculated. First of all, it is known that instantaneous chip thickness is changing under the effect of vibrations generated at the present and previous tool positions. The vibrations in the feed direction are parallel to the chip thickness whereas the radial vibrations are perpendicular to them. Actual radial depth of cut is found to be;

$$a_d = \bar{a} + \tilde{a} \tag{4.14}$$

where $\bar{a}$ and $\tilde{a}$ are intended radial depth of cut and radial vibration amplitudes, respectively. Actual uncut chip thickness along the feed direction is found to be;

$$c_d = \bar{c} + \tilde{c} \tag{4.15}$$

where $\bar{c}$ and $\tilde{c}$ are intended uncut chip thickness and vibration amplitudes in feed direction, respectively. After the actual radial depth of cut and uncut chip thickness values are obtained, current dynamic chip load is calculated. And finally, by using the dynamic chip load values, dynamic cutting forces in radial, feed and tangential directions are calculated.

### 4.7 Surface Roughness in Turning

Functional requirements and reliability of a machined part such as its load carrying capacity, friction, wear and lubrication characteristics, corrosion resistance, and fatigue life are affected by the surface finish of the machined part. Therefore, the relationship between the process parameters and the resultant surface finish is very important in machining processes. The accuracy of the manufactured part with respect to the dimensions specified by the designer determines the quality of the machined surface. Every machining operation leaves characteristic marks on the machined surface. This evidence is in the form of finely spaced micro irregularities left by the cutting tool. Each type of cutting tool leaves its own individual pattern, which is known as surface finish or surface roughness. Roughness consists of surface irregularities which result from the various machining process. These irregularities combine to form surface texture. Roughness height is the height of the irregularities with respect to a reference line.

The combination of ideal roughness and natural roughness produced by a machining process ends up with the resultant roughness. Ideal surface roughness is a function of only feed and geometry. It represents the best possible finish which can be obtained for a given tool shape and feed. It can be achieved only if the built-up-edge, chatter and inaccuracies in the machine tool movements are eliminated completely. According to Armarego [58], the surface finish in turning operations is depicted by the peak-to-valley height. The ideal surface roughness was represented by predictive equations incorporating the feed, depth of cut and tool profile geometry such as $\psi_r, \kappa_r'$, and $r$. In Figure 4.3 the general terms used in surface finish equations are shown. In Figure 4.4, the way of the calculation of the surface roughness is briefly described.

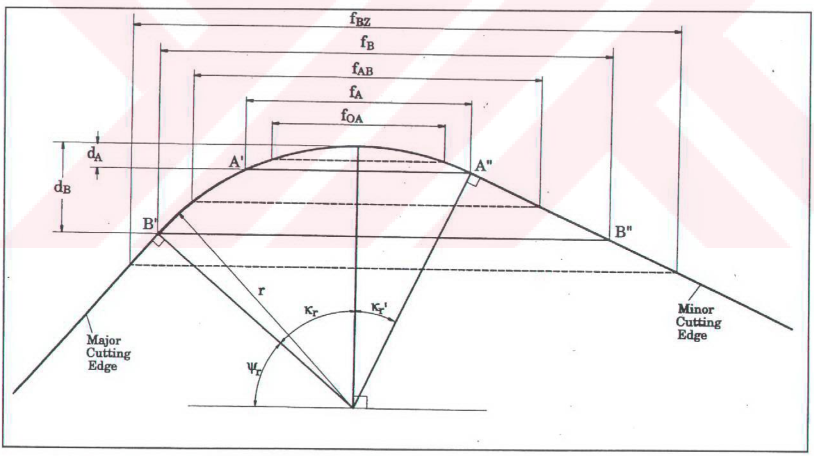


Figure 4.3: Ideal feed marks and peak to valley values, adopted from Armarego [58].

The calculation of the parameters in Figure 4.4 is shown in the following equations. The true area of cut calculations can be found in Armarego [58] for further interested readers.

Depth Limits:

$$d_A = r.(1-\cos\kappa_r')$$
$$d_B = r.(1-\sin\psi_r) = r.(1-\cos\kappa_r)$$

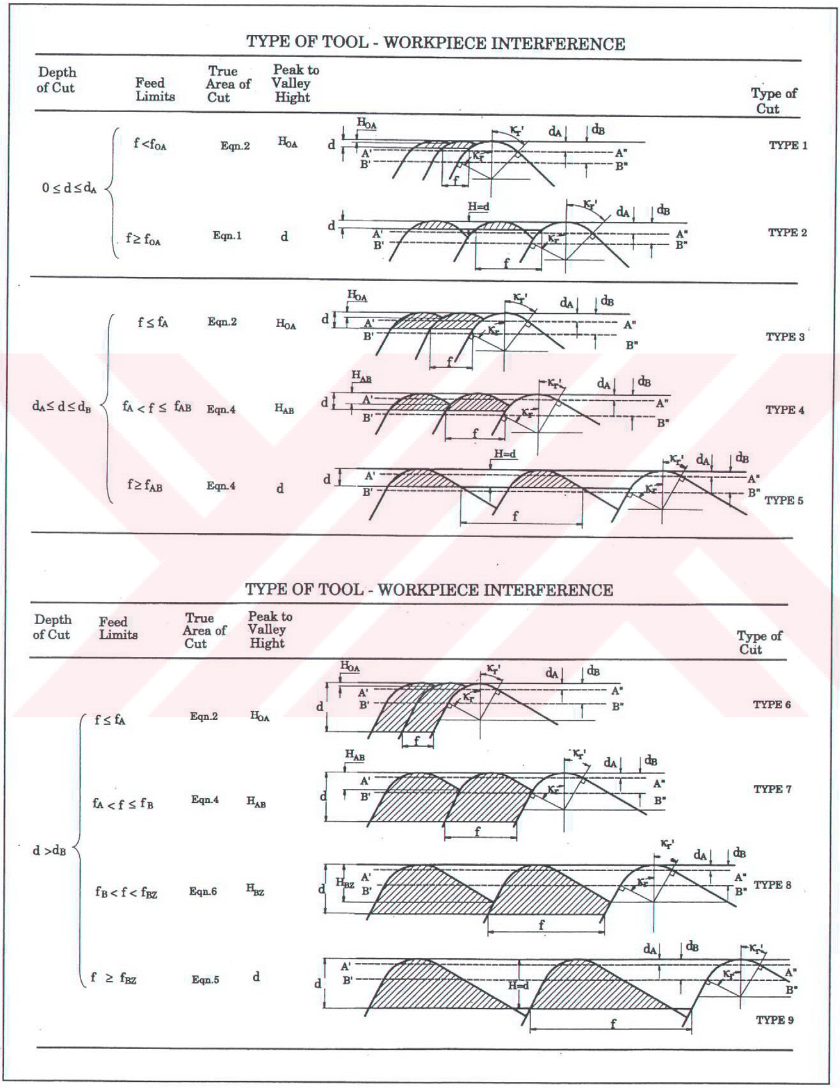


Figure 4.4: Ideal feed and depth of cut limits, adopted from Armarego [58].

Feed Limits and Coressponding Depth of Cut (d) Limits:

$$f_{OA} = 2.\sqrt{2.r.d - d^2}$$
$$f_A = 2.r.\sin\kappa_r'$$
$$f_{AB} = \sqrt{2.r.d - d^2} + r.\sin\kappa_r' + \cot\kappa_r'.[d - r.(1-\cos\kappa_r')]$$
$$f_B = \frac{r.[1-\cos(\kappa_r - \kappa_r')]}{\sin\kappa_r'}$$
$$f_{BZ} = \frac{r.[1-\sin(\psi_r - \kappa_r')]}{\sin\kappa_r'} + [d - r.(1-\sin\psi_r)].(\cot\kappa_r' + \tan\psi_r)$$

Peak to Valley Height:

$$H_{OA} = r - \frac{\sqrt{4.r^2 - f^2}}{2}$$
$$H_{AB} = r.(1-\cos\kappa_r') + f.\cos\kappa_r'.\sin\kappa_r' - \sqrt{2.f.r.\sin^3\kappa_r' - f^2.\sin^4\kappa_r'}$$
$$H_{BZ} = \frac{r.[\cos(\psi_r - \kappa_r') - \sin\kappa_r' - \cos\psi_r] + f.\sin\kappa_r'.\cos\psi_r}{\cos(\psi_r - \kappa_r')}$$

In practice, it is not usually possible to achieve conditions such as those described above, and normally the natural surface roughness forms a large proportion of the total roughness. One of the main factors contributing to natural roughness is the occurrence of a built-up edge. Thus, larger the built up edge, the rougher would be the surface produced, and factors tending to reduce chip-tool friction and to eliminate or reduce the built-up edge would give improved surface finish.

Whenever two machined surfaces come in contact with one another, the quality of the mating parts plays an important role in the performance and wear of the mating parts. The height, shape, arrangement and direction of these surface irregularities on the workpiece depend upon a number of factors such as cutting speed, feed, depth of cut, tool geometry (nose radius, rake angle, side cutting edge angle), vibrations between workpiece and cutting tool, workpiece and tool material combination and their mechanical properties, quality and type of the machine tool used.

## 4.8 Simulations

### 4.8.1 Cutting Force Simulations

The dynamic simulations were performed for the cutting speed values between 90 and 140 m/min, and for the radial depths of cut between 0.06 and 0.12 mm. Feedrate was constant at 0.12 mm/rev for all tests. Frequency response functions of the tool and turret system along the radial and feed directions were measured and they are shown in Figure 4.5 and Figure 4.6. From the measured frequency response functions, modal parameters of the system were determined and they are presented in Table 4.1. As observed in Table 4.1, the stiffness values at the natural frequencies of the system are quite high. This is very much desirable in the hard turning process due to the fact that minimum dynamic vibration is required. When simulations for the above cutting conditions were performed, it was seen that the dynamic components of the cutting forces (Figure 4.7) are negligible if they are compared with the static components of the cutting forces. However due to the static components of the cutting forces, the static deflections coming from the dynamic model are between 0.3-0.5 microns as seen in Figure 4.8. Dynamic vibration values which are also very small can be seen in Figure 4.9.

Table 4.1: Modal parameters

| | Radial Direction | | | |
|---|---|---|---|---|
| Mode | $\omega_n$ [Hz] | $\zeta$ | k [N/m] | Residue [m/N] |
| 1 | 306 | 0.044 | 1.63E+08 | 9.62E-06 |
| | Feed Direction | | | |
| Mode | $\omega_n$ [Hz] | $\zeta$ | k [N/m] | Residue [m/N] |
| 1 | 731 | 0.04787 | 2.96E+08 | 7.772E-06 |

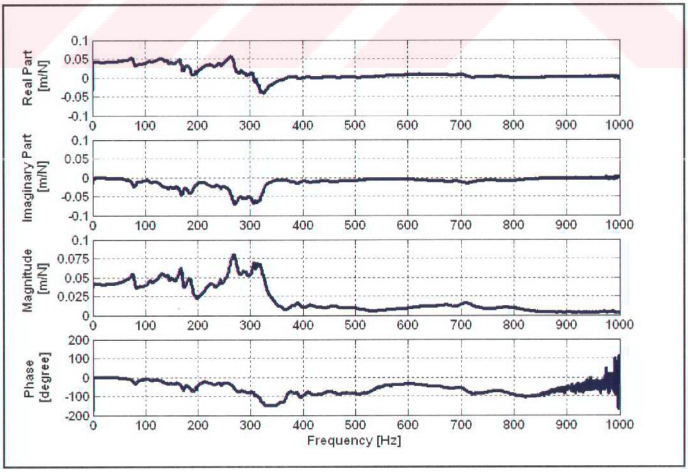


Figure 4.5: Frequency Response Function of the system in radial direction.

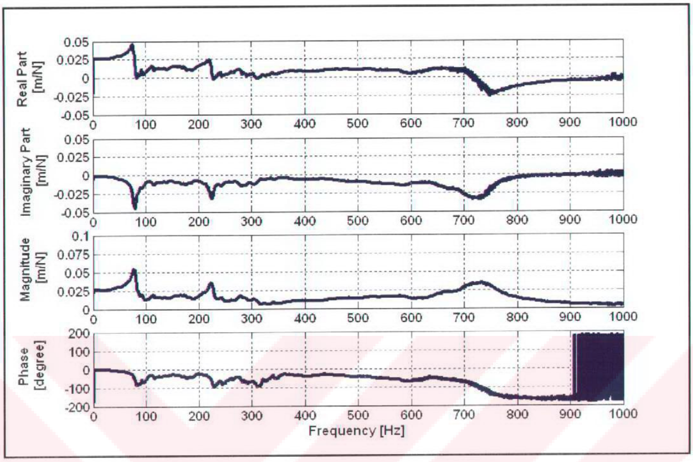


Figure 4.6: Frequency Response Function of the system in feed direction.

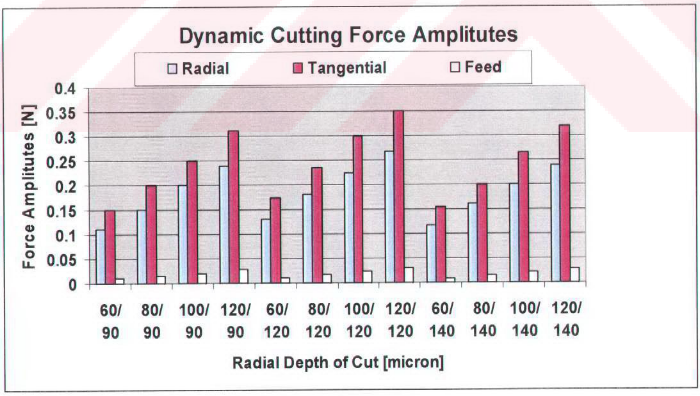


Figure 4.7: Dynamic cutting force amplitudes.

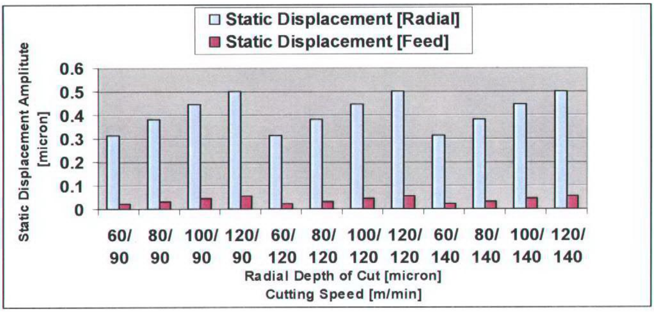


Figure 4.8: Static displacement amplitudes.

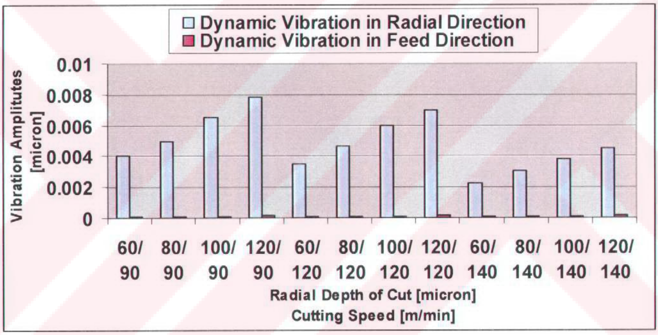


Figure 4.9: Vibration amplitudes.

### 4.8.2 Roughness Simulations

Roughness and waviness measurements were performed on the induction hardened 50CrV4 workpiece by using a perthometer. The machining operation was performed on Monfort 400 RNC Plus CNC turning machine with a cutting speed value of 140 m/min, radial depth of cut of 0.2 mm and feedrate of 0.08 mm/rev. The cutting inserts used in the calibrations were Seco CBN 10. The measured surface profile of the workpiece is shown on Figure 4.10.

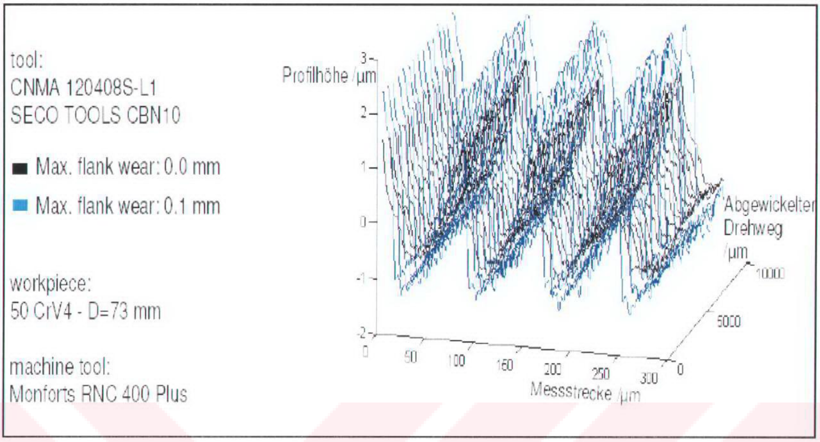


Figure 4.10: Workpiece surface profile.

The profile shape for the first revolution is shown in Figure 4.11**.** The average profile depth was measured to be 2 [µ] from the Figure 4.11.

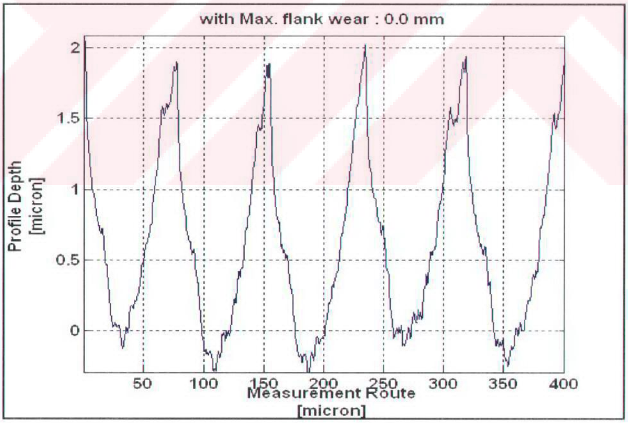


Figure 4.11: Profile depth.

In order to find the total surface roughness, first of all ideal surface roughness was calculated by using the formulations given in Section 4.3. Side cutting edge angle $\psi_r$ and end cutting edge angle $\kappa_r'$ of the insert was found as 36.8° and 37.3°, respectively, as shown in Figure 4.12.

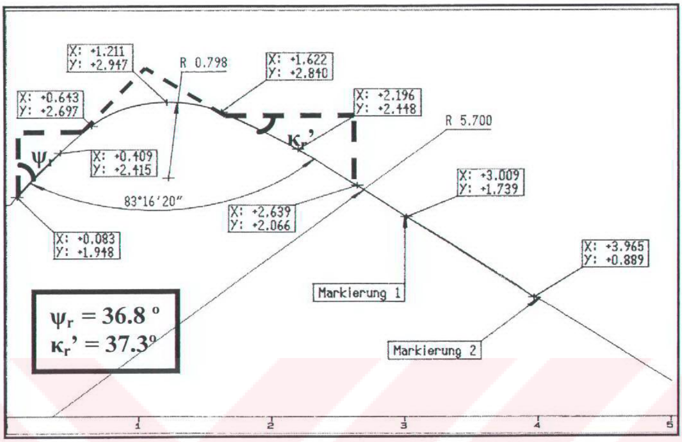


Figure 4.12: Prediction of side cutting edge angle $\psi_r$ and end cutting edge angle $\kappa_r'$.

Depth of cut limits, dA and dB (Figure 4.4) were found to be 0.1636, and 0.3208 respectively. Depth of cut, d, was equal to 0.2 mm, and feedrate, f, was equal to 0.08 mm. Thus, $dA < d < dB$. Feed limit, $F_A$, was found to be 0.9696 and since $f < F_A$ the corresponding type of cut was found to be as Type 6. Peak to valley height was found to be as $H_{OA}$, which is $1\,\mu$.

In order to find natural surface roughness, the dynamic simulations were performed for the same cutting conditions. The forces in the radial, tangential and feed directions were calculated to be 89.2 N, 90.0 N and 25.1 N with dynamic components of 0.325 N, 0.45 N, and 0.05 N, respectively. The amplitude of the static displacement in radial direction was found to be 0.55 $\mu$, while in feed direction it was found to be $0.085\,\mu$ with dynamic vibration amplitudes of $0.007\,\mu$ and $0.00025\,\mu$, respectively. When the static displacement value is summed up with the scallop height due to kinematics of the process, a surface profile depth of $1.55\,\mu$ is calculated, which is very close to the experimentally measured one.

# Chapter 5

# TEMPERATURE PREDICTIONS IN HARD TURNING

## 5.1 Introduction

In this chapter, tool, chip, and workpiece temperature fields in hard turning operation are predicted by using a numerical model based on finite difference method. Hard turning is studied by modeling the heat transfer between tool, chip and workpiece. The shear energy created in the primary zone, the friction energy produced at the rake face - chip contact zone, the heat balance between the moving chip and stationary tool, and moving chip and workpiece are considered. The temperature distribution is solved using finite difference method. The simulation results are in satisfactory agreement with experimental temperature measurements reported in the literature.

## 5.2 The Heat Balance Equation

Based on the first law of thermodynamics, the energy conservation law, can be stated as: "The rate at which thermal and mechanical energy enters to a control volume, plus the rate at which thermal energy is generated within the control volume, minus the rate at which thermal and mechanical energy leaves the control volume must equal to the rate of increase of energy stored within the control volume".

$$\dot{E}_{in} + \dot{E}_{generated} - \dot{E}_{out} = \dot{E}_{stored} \tag{5.1}$$

The purpose of the heat conduction analysis is to determine temperature field based on given boundary conditions in a medium. Let us assume a homogeneous medium and assume that temperature field is expressed in Cartesian coordinates as $T(x, y, z)$. Considering an infinitesimal differential control volume, $dx.dy.dz$, as shown in Figure 5.1, if there are temperature gradients, the heat conduction will occur. Let us assign $q_x, q_y, \text{and } q_z$ as the heat conduction rates which are perpendicular to each control surface as shown in Figure 5.1. Using Taylor series expansion and ignoring the higher order terms, heat flow rates in the three orthogonal directions can be written as first order approximations:

$$q_{x+dx} = q_x + \frac{\partial q_x}{\partial x} dx$$
$$q_{y+dy} = q_y + \frac{\partial q_y}{\partial y} dy \qquad (5.2)$$
$$q_{z+dz} = q_z + \frac{\partial q_z}{\partial z} dz$$

The first line of the above equation can be interpreted as the statement of the heat conduction rate at $x + dx$ is equal to the value of this component at $x$ plus the differential heat conduction changes with respect to $x$.

Energy conversation equation can be rewritten as

$$\underbrace{q_x + q_y + q_z}_{\text{Heat Input}} + \underbrace{\dot{q}dxdydz}_{\text{Heat Generated}} \underbrace{- q_{x+dx} - q_{y+dy} - q_{z+dz}}_{\text{Heat Output}} = \underbrace{\rho c_p \frac{\partial T}{\partial t} dxdydz}_{\text{Heat Stored}} \qquad (5.3)$$

and in partial differential form:

$$-\frac{\partial q_x}{\partial x} dx - \frac{\partial q_y}{\partial y} dy - \frac{\partial q_z}{\partial z} dz + \dot{q}\, dxdydz = \rho c_p \frac{\partial T}{\partial t} dxdydz \qquad (5.4)$$

The heat conduction rates can be evaluated from the Fourier's Heat Conduction Law,

$$q_x = -kdydz \frac{\partial T}{\partial x}$$
$$q_y = -kdxdz \frac{\partial T}{\partial y} \qquad (5.5)$$
$$q_z = -kdxdy \frac{\partial T}{\partial z}$$

Therefore the heat balance equation becomes

$$\frac{\partial (k \frac{\partial T}{\partial x})}{\partial x} + \frac{\partial (k \frac{\partial T}{\partial y})}{\partial y} + \frac{\partial (k \frac{\partial T}{\partial z})}{\partial z} + \dot{q} = \rho c_p \frac{\partial T}{\partial t} \qquad (5.6)$$

Assuming that the heat conduction coefficient does not vary in the medium,

$$\frac{\partial^2 T}{\partial x^2} + \frac{\partial^2 T}{\partial y^2} + \frac{\partial^2 T}{\partial z^2} + \frac{\dot{q}}{k} = \frac{1}{\alpha} \frac{\partial T}{\partial t} \qquad (5.7)$$

where $\alpha$ is the thermal diffusivity defined as $\frac{k}{\rho c_p}$.

Similar to the derivation procedure used for the Cartesian coordinates above, the heat balance, in polar coordinates, will be defined using the control volume, $dr, d\psi, dz$, shown in Figure 5.1 and the general form of the heat equation in Polar coordinates is obtained as following:

$$\frac{1}{r}\frac{\partial}{\partial r}(k \frac{\partial T}{\partial r}) + \frac{1}{r^2}\frac{\partial}{\partial \psi}(k \frac{\partial T}{\partial \psi}) + \frac{\partial}{\partial z}(k \frac{\partial T}{\partial z}) + \dot{q} = \rho c_p \frac{\partial T}{\partial t} \qquad (5.8)$$

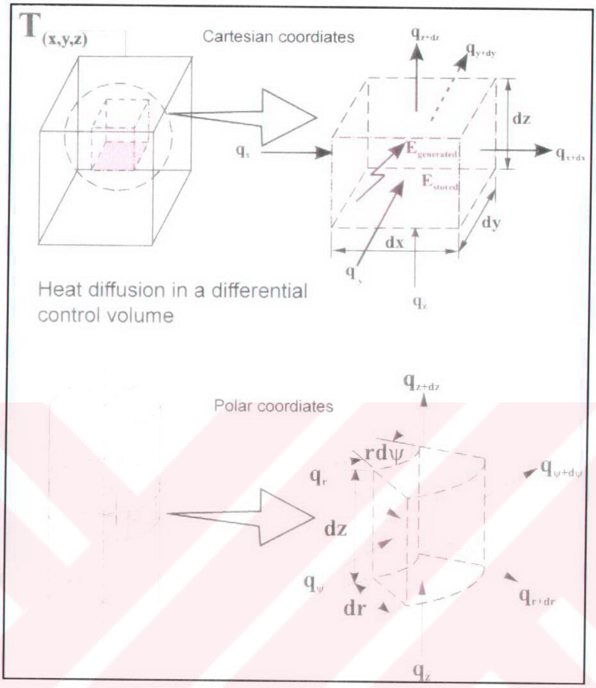


Figure 5.1: Heat diffusion in differential control zones defined in Cartesian and Polar coordinates.

### 5.3 Finite Difference Form of the Heat Balance Equations

Although analytical formulations are available, and may be used for the solution of two dimensional, steady-state conduction problems with simplified geometry and boundary conditions, in general, it is not always practical and even possible to apply analytical techniques to the complicated geometries and boundary conditions. In these cases, numerical techniques such as finite-difference, finite-element or boundary element methods can be quite profound. In our model, finite difference method is used.

In the analytical formulations and solutions of heat transfer problems, temperature fields are continuous. In the finite difference form formulation of the problem, the medium is subdivided into small regions as shown in Figure 5.2. These small regions or discrete elements are called meshes, grids or nodal networks.

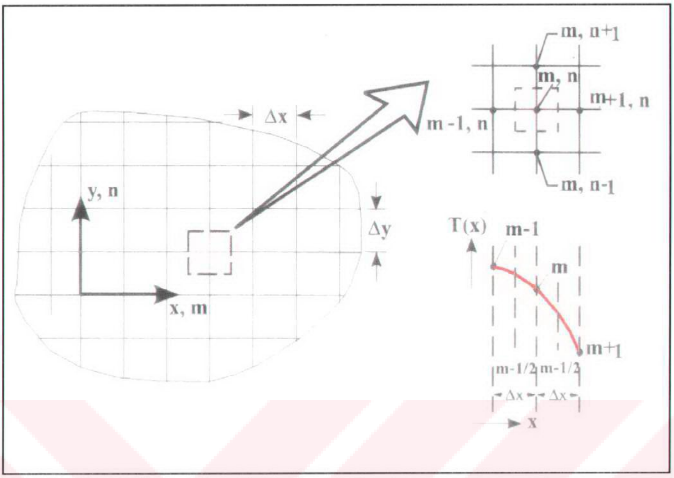


Figure 5.2: Illustration of nodal network in 2-D control volume and finite difference approximation.

The positions of the nodal points are denoted by $x$ and $y$ in the local medium coordinates, and indices of the nodal points are represented by $m$ and $n$ along these axes, respectively. If the medium is divided into small meshes with sizes of $\Delta x$ and $\Delta y$ along the $x$ and $y$ directions, respectively, then the following approximations of the partial derivatives can be found for two-dimensional medium,

$$\left.\frac{\partial T}{\partial x}\right|_{m-\frac{1}{2},n} \approx \frac{T_{m,n} - T_{m-1,n}}{\Delta x}$$
$$\left.\frac{\partial T}{\partial x}\right|_{m+\frac{1}{2},n} \approx \frac{T_{m+1,n} - T_{m,n}}{\Delta x} \tag{5.9}$$

The second partial derivatives for the internal nodes can be written as,

$$\left.\frac{\partial^2 T}{\partial x^2}\right|_{m,n} \approx \frac{\left.\frac{\partial T}{\partial x}\right|_{m+1/2,n} - \left.\frac{\partial T}{\partial x}\right|_{m-1/2,n}}{\Delta x} \tag{5.10}$$

By substituting Equation 5.9 into the Equation 5.10 leads to:

$$\left.\frac{\partial^2 T}{\partial x^2}\right|_{x,y} \approx \frac{T_{m+1,n} + T_{m-1,n} - 2T_{m,n}}{\Delta x^2} = \frac{T_{(x+\Delta x,y)} + T_{(x-\Delta x,y)} - 2T_{(x,y)}}{\Delta x^2} \tag{5.11}$$

Similarly, the second partial derivative with respective to $y$ can be determined as,

$$\left.\frac{\partial^2 T}{\partial y^2}\right|_{x,y} \approx \frac{T_{m,n+1} + T_{m,n-1} - 2T_{m,n}}{\Delta y^2} = \frac{T_{(x,y+\Delta y)} + T_{(x,y-\Delta y)} - 2T_{(x,y)}}{\Delta y^2} \tag{5.12}$$

The above derivations were for Cartesian coordinates. In a similar fashion, the following results can be determined in terms of Polar coordinate parameters,

$$\begin{aligned} \left.\frac{\partial^2 T}{\partial r^2}\right|_{x,\psi} &= \frac{T_{(r+\Delta r,\psi)} + T_{(r-\Delta r,\psi)} - 2T_{(r,\psi)}}{\Delta r^2} \\ \left.\frac{1}{r}\frac{\partial T}{\partial r}\right|_{x,\psi} &= \frac{T_{(r+\Delta r,\psi)} + T_{(r-\Delta r,\psi)} - 2T_{(r,\psi)}}{2r\Delta r} \\ \left.\frac{1}{r^2}\frac{\partial^2 T}{\partial \psi^2}\right|_{x,\psi} &= \frac{T_{(r,\psi+\Delta\psi)} + T_{(r,\psi-\partial\psi)} - 2T_{(r,\psi)}}{r^2\Delta\psi^2} \end{aligned} \tag{5.13}$$

## 5.4 Heat Generated in the Primary and Secondary Zones

In the temperature field predictions for the chip, tool and workpiece, which are based on the finite difference method utilized for hard turning operations, it is assumed that the process has orthogonal cutting geometry and the chip is sheared from the blank at an infinitely thin shear plane (i.e. primary deformation zone)(Figure 5.3). The chip slides on the rake face (i.e. secondary deformation zone) with a constant average friction coefficient.

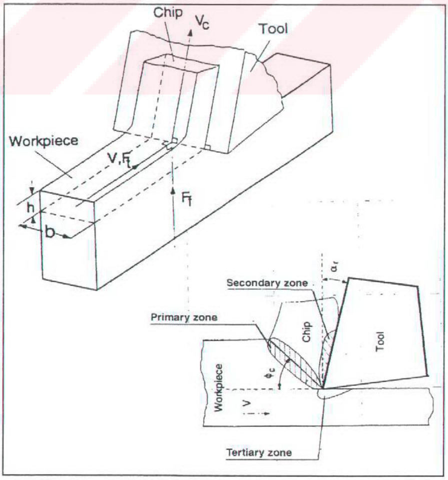


Figure 5.3: Orthogonal cutting geometry and deformation zones, adopted from Altintas [57].

Heat generated per unit depth of cut in the primary and secondary zones are given as follows, respectively, [57]

$$\dot{Q}_s = F_s V_s = \frac{\tau.h.V_w.\cos(\alpha_n)}{\sin(\phi_n)\cos(\phi_n - \alpha_n)}$$
$$\dot{Q}_f = F_f V_c = \frac{\tau.h.V_w.\sin(\beta_n)}{\cos(\phi_n + \beta_n - \alpha_n)\sin(\phi_n - \alpha_n)} \tag{5.14}$$

where $F_s, F_f, V_w, V_s$ and $V_c$ are the shear force in the shear plane, the frictional force between the tool rake face and the chip contact zone, the cutting velocity, the cutting velocity component along the shear plane and the cutting velocity component along the rake face, respectively. $\tau, \phi_n, \alpha_n$ and $\beta_n$ are the shear stress in the shear plane, shear angle, normal rake angle and normal friction angle, respectively. $h$ is the instantaneous uncut chip thickness ($h =$ feed per revolution for turning).

The average temperature rise of the chip per unit depth of cut due to the shearing is determined by Oxley's energy partition function [29]

$$\Delta\overline{T} = \dot{Q}_s(1-\chi)/(\rho.c_c.h.V_w) \tag{5.15}$$

where $\rho$ and $c_c$ are the mass density and specific heat capacity of the chip, respectively. $\chi$ represents the proportion of the shearing flux entering into the workpiece, and is defined by:

$$\chi = 0.5 - 0.35\log_{10}(R_t, \tan(\phi_n)) \quad \text{for} \quad 0.004 \le R_t.\tan(\phi_n) \le 10$$
$$\chi = 0.5 - 0.15\log_{10}(R_t, \tan(\phi_n)) \quad \text{for} \quad R_t.\tan(\phi_n) \ge 10 \tag{5.16}$$

where $R_t = h.V_w / \zeta$ is the thermal number. $\zeta$ is the thermal diffusivity defined as $k/(\rho.c)$ in which $k, \rho, c$ represent conductivity, mass density and specific heat capacity of medium, respectively.

The average temperature rise on the shear plane is used as a boundary condition at Point D in Figure 5.4, and the heat generated in the primary and secondary zones are used as heat sources in solving the temperature distribution within the tool, chip and workpiece as presented in the following section.

### 5.5 Chip Temperature Model

The chip can be considered as a medium which is in quasi-static thermal equilibrium during an infinitesimal time. By considering orthogonal cutting (Figure 5.3), with two-dimensional heat flow and one-dimensional mass transfer, the heat balance equation for the discrete chip zone can be written in the finite difference form in Cartesian coordinates as the following ,

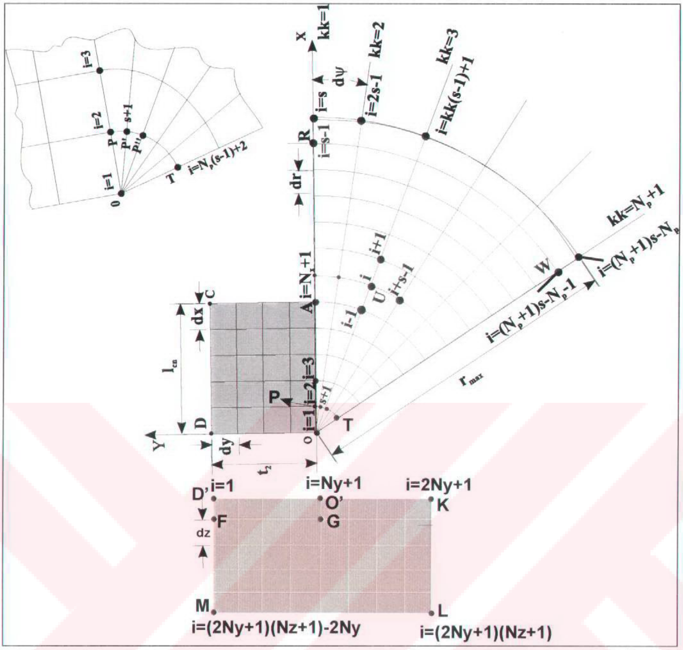


Figure 5.4: Illustration of chip, tool and workpiece meshing.

$$\frac{T_c(x+\partial x,y)+T_c(x-\partial x,y)-2T_c(x,y)}{\delta x^2}+\frac{T_c(x,y+\partial y)+T_c(x,y-\partial y)-2T_c(x,y)}{\delta y^2}+Q_c(x,y)=\frac{\rho.c_c}{k_c}.V_c.\frac{\partial T_c}{\partial x} \quad (5.17)$$

where $Q_c, k_c, c_c$ are also the energy generation rate per unit area in the differential chip zone, thermal conductivity and specific heat capacity of the chip, respectively.

The chip geometry must be meshed into small discrete elements for the finite difference solution of the chip temperature field and the equilibrium equation above needs to be written for each nodal point of the chip. The aspect ratio of the mesh can be unity to simplify the solutions, $\delta x = \delta y$.

In the equilibrium equation (Equation 5.17), the heat flow into the differential chip control zone $(Q_c)$ from the frictional heat source can be localized for each node along the chip-tool contact length as:

$$Q_{c(i)} = (1-B_i).Q_f\ .dx / l_{cn}k_c \text{ if and only if } 1 \le i \le N_x + 1 \quad (5.18)$$

where $B_i$ represents the proportion of the frictional heat flowing into the tool at the $i^{th}$ nodal point and it is unknown, initially. $\dot{Q}_f$, $l_{cn}$ and $N_x$ are the frictional heat generation rate, chip tool contact length and number of grids along the x axis, respectively. It should be noticed that a uniform heat generation was considered along the chip-tool contact length. The internal nodes (all nodes other than $1 \le i \le N_x + 1$) will physically have no heat generation input. Therefore, $\dot{Q}_{c(i)}$ will be zero for all these nodes. Equilibrium equations for all of the nodes of the chip can be written as shown in Equation 5.17, and all these equilibrium equations can be collected in a compact matrix form, and therefore, the temperature of each nodal point in the chip nodal network corresponds to a value in the chip temperature array $\{T_c\}$ can be determined as:

$$[A].\{T_c\} = \{C\} \quad \rightarrow \quad \{T_c\} = [A]^{-1}.\{C\} \tag{5.19}$$

where $[A]$ is the square coefficient matrix determined from Equation 5.17, $\{T_c\}$ is the chip temperature array with size of $(N_y + 1)(N_x + 1)$ (where $N_y$ is the number of meshes along the y axis as shown in Figure 5.4), and $\{C\}$ is the heat generation array. Writing the equilibrium equation for each nodal point $(1 \le i \le (N_y + 1).(N_x + 1))$ leads to the following elements of coefficient matrix, $[A]$, and heat generation array, $\{C\}$;

<u>For Node at Point O:</u>

$A(i,i) = -1; A(i,i+1) = 2/G; A(i,N_x + 2) = 2/G; C(i) = -\dot{Q}_c(i)/G;$

<u>For Nodes between Points O and A:</u>

$A(i,i) = -1; A(i,i+1) = (1-H)/G; A(i,i-1) = (1+H)/G; A(i,i+N_x+1) = 2/G; C(i) = -\dot{Q}_c(i)/G;$

<u>For Node at Point A:</u>

$A(i,i) = -1; A(i,i-1) = 2/G; A(i,i+N_x+1) = 2/G; C(i) = -\dot{Q}_c(i)/G;$

<u>For Nodes between Points A and C:</u>

$A(i,i) = -1; A(i,i-1) = 2/G; A(i,i+N_x+1) = 1/G; A(i,i-N_x-1) = 1/G; C(i) = 0;$

For Node at Point C:

$A(i,i)=-1; A(i,i-1)=2/G; A(i,i-N_x-1)=2/G; C(i)=0;$

For Nodes between Points C and D:

$A(i,i)=-1; A(i,i+1)=(1-H)/G; A(i,i-1)=(1+H)/G; A(i,i-N_x-1)=2/G; C(i)=0;$

For Node at Point D:

$A(i,i)=0; A(i,i+1)=2/G; A(i,i-N_x-1)=2/G; C(i)=T_{AB};$

For Nodes between D and O:

$A(i,i)=-1; A(i,i+1)=2/G; A(i,i+N_x+1)=1/G; A(i,i-N_x-1)=1/G; C(i)=0;$

For Internal Grids:

$A(i,i)=-1; A(i,i+1)=(1-H)/G; A(i,i-1)=(1+H)/G; A(i,i+N_x+1)=1/G; A(i,i-N_x-1)=1/G;$
$C(i)=0;$

where $H=\dfrac{\rho.c.\delta x}{2.k_w}$; $G=4$; $T_{AB}=T\_room+\overline{\Delta T}$.

It should be noticed that point D is on the shear plane and its temperature is to be set as initial workpiece temperature plus the average temperature increment, $(\overline{\Delta T})$, (defined in Equation 5.15), due to shearing.

### 5.6 Tool Temperature Model

Whereas Cartesian coordinates are used for the chip, applying polar coordinates to the tool is advantageous due to the mathematical accuracy and its convenience in the computational implementation of the model. The heat transfer equilibrium equations for the control zone around the tool nodal points can be written in the finite difference form in polar coordinates as the following;

$$\frac{T_{t(r+\delta r,\psi)}+T_{t(r-\delta r,\psi)}-2T_{t(r,\psi)}}{\delta r^2}+\frac{T_{t(r+\delta r,\psi)}-T_{t(r-\delta r,\psi)}}{2r\delta r}+\frac{T_{t(r,\psi+\delta\psi)}+T_{t(r,\psi-\delta\psi)}-2T_{t(r,\psi)}}{r^2\delta\psi^2}+\dot{Q}_t=0 \quad (5.20)$$

where $T_t$ represents the tool temperature field, $r$ is the radial distance between the nodal point in concern and the tool tip shown as point O in Figure 5.4, and $\psi$ is the angular position of the nodal point. $k_t$ and $\dot{Q}_t$ denote the tool thermal conductivity and heat generation rate per unit area in the control zone, respectively.

The frictional heat flow rate into the tool is given by

$$\dot{Q}_{t(i)} = (B_i.\dot{Q}_f.\delta x)/l_{cn}.k_t \qquad \text{if and only if } 1 \le i \le N_x + 1 \tag{5.21}$$

Similar to the chip heat balance equations, the equilibrium equations for all nodal points of the tool can be written and collected in a compact form, and therefore, the tool temperature distribution can be determined from

$$[D].\{T_t\} = \{E\} \quad \rightarrow \quad \{T_t\} = [D]^{-1}.\{E\} \tag{5.22}$$

where $[D]$ is the square coefficient matrix determined from Equation 5.28, $\{T_t\}$ is the tool temperature array, $\{E\}$ is the heat generation array for the tool.

If the same procedure defined in Cartesian coordinates is followed and the finite difference equilibrium equation of the tool (Equation 5.20) is written for each nodal point of the tool in Polar coordinates, to the following elements of coefficient matrix, $[A]$, and heat generation array, $\{C\}$ is obtained;

For Nodes between Points O and A:

$D(i,i) = C_1;\ D(i,i+1) = C_2;\ D(i,i-1) = C_3;\ D(i,i+s-2) = 2.C_4;\ E(i) = \dot{Q}_t(i).C_6;$

For Nodes between Points A and R:

$D(i,i) = C_1;\ D(i,i+1) = C_2;\ D(i,i-1) = C_3;\ D(i,i+s-2) = C_4 + C_5;\ E(i) = 0;$

For Nodes at Point R:

$D(i,i) = C_1;\ D(i,i-1) = C_3;\ D(i,i+s-2) = C_4 + C_5;\ E(i) = -C_2.T\_back;$
where $T\_back = T\_room$ .

For Nodes between Points R and W:

$D(i-kk,i-kk) = C_1;\ D(i-kk,i-kk-1) = C_3;\ D(i-kk,i-kk-s+2) = C_4; D(i-kk,i-kk+s-2) = C_5;$
$E(i-kk) = -C_2.T\_back;$
where $kk = \text{floor}((i-1)/(s-1))$

For Nodes between Points P and T:

$D(i-kk,i-kk) = C_1;\ D(i-kk,i-kk+1) = C_2;\ D(i-kk,1) = C_3; D(i-kk,(kk+1).(s-2)+2) = C_4;$
$D(i-kk,(kk-1).(s-2)+2) = C_5;\ E(i-kk) = 0;$

For Node at Point T:

$D(i-kk,i-kk)=C_1;\ D(i-kk,i-kk+1)=C_2;\ D(i-kk,1)=C_3; D(i-kk,i-kk-s+2)=C_4+C_5;$
$E(i-kk)=0;$

For Nodes between T and W:

$D(i-kk,i-kk)=C_1;\ D(i-kk,i-kk+1)=C_2;\ D(i-kk,i-kk-1)=C_3; D(i-kk,i-kk-s+2)=C_4+C_5;$
$E(i-kk)=0;$

For Node at Point W:
$D(i-kk,i-kk)=C_1;\ D(i-kk,i-kk-1)=C_3;\ D(i-kk,i-kk-s+2)=C_4+C_5; E(i-kk)=-C_2.T\_back;$

For Node at Point O:

$D(i,i)=-(N_p+1)/\delta r^2; D(i,2:s-1:N_p.(s-1)+2)=1/\delta r^2; E(i)=q_t(i).C_7;$

For Internal Nodes:

$D(i-kk,i-kk)=C_1;\ D(i-kk,i-kk+1)=C_2;\ D(i-kk,i-kk-1)=C_3; D(i-kk,i-kk+s-2)=C_4;$
$D(i-kk,i-kk-s+2)=C_5;\ E(i-kk)=0;$

where

$$C_1=-2;$$

$$C_2=\frac{(2.r_i+\delta r).(r_i.\delta\psi^2)}{2.(r_i^2.\delta\psi^2+\delta r^2)};$$

$$C_3=\frac{(2.r_i-\delta r).(r_i.\delta\psi^2)}{2.(r_i^2.\delta\psi^2+\delta r^2)};$$

$$C_4=\frac{\delta r^2}{2.(r_i^2.\delta\psi^2+\delta r^2)};$$

$$C_5=C_4;$$

$$C_6=\frac{r_i.\delta r.\delta\psi}{2.(r_i^2.\delta\psi^2+\delta r^2)};$$

$$C_7=\frac{\delta r^2.\delta\psi}{(\delta r^2.\delta\psi^2+\delta r^2)}.$$

$\delta r, \delta\psi$ are the grid lengths in radial and angular directions, respectively, and $r_i$ is the distance of the $i^{th}$ node to the tool tip point.

In the above equations besides the tool and chip temperature distribution, the partitions of the heat ($B_i$) at the nodal points along the chip workpiece contact length are not known initially. Therefore, an iterative process is required for the computation. Initial values between 0 and 1 can be assigned for the heat partition at each nodal point. The tool and chip temperature fields can be determined based on the initial assignment of $B_i$. After solving the chip and tool heat balance equations (Equation 5.17, Equation 5.20), if temperatures of the corresponding tool and chip nodal points, at which tool and chip are in contact, are different than each other, then the heat partition value for the corresponding nodal points needs to be modified. The following formulation can be employed for the partition modification,

$$dB_i(1:N_x+1)=\frac{(T_c(1:N_x+1)-T_c(1:N_x+1))}{\dfrac{(T_c(1:N_x+1)+T_c(1:N_x+1))}{2}} \tag{5.23}$$

Essentially, the above equation is comparing the difference between the chip and tool temperatures at every nodal point, at which chip and tool is in contact, with their average temperature. If maximum of $dB_i$ is greater than a certain predefined percentage (for instance %1), then the new heat partition value for the corresponding node can be assigned as $B_i = B_i + dB_i$.

With this new heat partition, the finite difference equations for the chip, and tool are resolved, and new $dB_i$ is determined. The new partition should allow the temperature fields of tool and chip at the contact region to converge each other. This iterative solution will continue until maximum of $dB_i$ reaches to a predefined satisfactory low level. Thus, at the end of the iterative solution, the temperature fields of the tool and chip can be determined from $\{T_t\},\{T_c\}$.

### 5.7 Workpiece Temperature Model

Considering the geometry of the system, a first order approximation can be done and the workpiece can be assumed as a rectangular body. Therefore; cartesian coordinates can be applied to the workpiece. Similar to chip heat balance equations, the equilibrium equations for all nodal points of the workpiece can be written and collected in a compact form. Workpiece temperature distribution can be determined from

$$[R]\{T_w\}=[S]\rightarrow\{T_w\}=[R]^{-1}.[S] \tag{5.24}$$

where $R$ is the square coefficient matrix determined by using Equation 5.17 for the corresponding regions, $\{T_w\}$ is the workpiece temperature array, $\{S\}$ is the heat generation array for the workpiece. The heat conducted into the work material can be found by using Oxley's energy partition function which is previously explained in Equation 5.15.

Temperatures of the nodes between points D′ and O′ are the same as the temperatures of the nodes between points D and O, because they are infect the same nodes. Therefore the simulation starts from the point O′.

For Node at Point O′:

$R(i,i) = -1;\ R(i,i+1) = (1-H)/G;\ R(i,i+2N_y+1) = 2/G;\ Q(i) = -(1+H)/G.T_c(1);$

For Nodes between Point O′ and K:

$R(i,i) = -1;\ R(i,i+1) = (1-H)/G;\ R(i,i-1) = (1+H)/G; R(i,i+2N_y+1) = 2/G;\ Q(i) = 0;$

For Node at Point K:

$R(i,i) = -1;\ R(i,i-1) = 2/G;\ R(i,i+2N_y+1) = 2/G;\ Q(i) = 0;$

For Node at Point F:

$R(i,i) = -1;\ R(i,i+1) = 2/G;\ R(i,i+2N_y+1) = 1/G;\ Q(i) = -1/G.Tc((N_x+1).(2.N_y+1-i)+1);$

For Nodes between Point F and G:

$R(i,i) = -1;\ R(i,i+1) = (1-H)/G;\ R(i,i-1) = (1+H)/G; R(i,i+2N_y+1) = 1/G;$
$Q(i) = -1/G.Tc((N_x+1).(2.N_y+1-i)+1);$

For Nodes between Point K and L:

$R(i,i) = -1;\ R(i,i-1) = 2/G;\ R(i,i+2N_y+1) = 1/G; R(i,i-2N_y-1) = 1/G; Q(i) = 0;$

For Nodes between Point D′ and M

$R(i,i) = -1;\ R(i,i+1) = 2/G;\ R(i,i+2N_y+1) = 1/G; R(i,i-2N_y-1) = 1/G; Q(i) = 0;$

For Nodes between Point M and L:

$R(i,i) = -1;\ R(i,i+1) = (1-H)/G;\ R(i,i-1) = (1+H)/G; R(i,i-2N_y-1) = 1/G;\ Q(i) = -1/G.T\_room;$

For Node at Point L:

$R(i,i) = -1;\ R(i,i-1) = 2/G; R(i,i-2N_y-1) = 2/G;\ Q(i) = -1/G.T\_room;$

For Internal Nodes:

$R(i,i) = -1;\ R(i,i+1) = (1-H)/G; R(i,i-1) = (1+H)/G; R(i,i-2N_y-1) = 1/G;\ R(i,i+2N_y+1) = 1/G;$
$Q(i) = 0.$

### 5.8 Simulations and Experimental Results

Besides the cutting forces, the temperature fields for tool, chip, and workpiece were also predicted using the finite difference model, and average rake face temperatures were experimentally measured. The hardware used in the thermal measurements was the Fire-1 Fiber-optic Ratio Pyrometer with the smallest available fiber diameter of 0.4 [mm]. The temperature measurement set up is shown in Figure 5.5. In Figure 5.6 the principle of workpiece oriented temperature measurement is shown. A fused silica fiber is used to transmit the radiation to the pyrometer from measuring positions with limited optical access. The two-color principle allows accurate measurements of absolute temperatures of surfaces with unknown emissivities if the assumption of a gray body behavior at the measurement wavelengths is valid. The minimum temperature which can be measured with the pyrometer is limited due to the small radiation energy at low temperatures given by Planck's law, the emissivity of the body and the size of measurement area. At present temperatures of low emissivity metallic surfaces with sizes of 0.4 mm can be measured down to 250 °C.

The measurement of temperatures with a high time resolution is possible with infrared radiation techniques. The electromagnetic radiation emitted by a surface is measured and the temperature is evaluated by applying a calibration function. The relationship between the radiant energy and the temperature of a surface is expressed by Planck's law. The temperature of a surface T can be calculated from the measured emissive power E at a specified wavelength if the spectral emissivity of the surface is known,

$$E = \varepsilon_\lambda \frac{h.c_0^{\,2}}{\lambda^5} \frac{2\pi}{e^{h/(\lambda KT)} - 1} \tag{5.25}$$

where $h$ is Planck's constant, $c_0$ is the speed of light in vacuum, k is the Boltzmann constant, $\lambda$ is wavelength, $\varepsilon_\lambda$ is emissivity at specific wavelength.

The infrared radiation which was emitted from the chip on the rake face was collected by the quartz fiber and transmitted to the pyrometer. Different fibers with diameters up to 0.1 [mm] could be used with the pyrometer. Quartz fibers have the advantages of high operating temperatures, high mechanical strength and small bend radii as required in machining operations. A damaged surface of a fiber can be re-polished very easily. The radiation was collimated inside the pyrometer housing with a lens and passes a dichroic beam-splitter which reflects more than 95 % of the radiation with a wavelength shorter than 1.76 [mm] and transmits more than 85 % with a wavelength longer than 1.95 [mm]. The interference filters had center wavelengths of 1.7 and 2.0 [mm], respectively. After passing the filters, the radiation was focused on the detectors with two lenses. These detectors had a two-stage Peltierelement, which cools them down to a temperature of -40 °C. The cooling reduced the detector noise which is necessary for the measurement of low temperatures. The signals of the detectors were amplified by variable gain low noise amplifiers. The gain was adjustable from 104 to 1011 [V/A] and the maximum bandwidth was 500 [kHz]. This means that a maximum time resolution of 2 [ms] was possible if an appropriate data acquisition is used.

The pyrometer Fire-1 has the unique advantages to measure accurate absolute temperatures of surfaces with unknown and varying emissivities. The chip is subject to a heat treatment during the cutting process and so a calibration of the pyrometer at the chip surface is not possible because the emissivity of the chip surface will change during the cutting process. The spectral surface emissivity during the experiment is unknown which means that no exact absolute temperature can be evaluated with a monochromatic pyrometer or a standard infrared camera. The concept of the two-color pyrometer was used to minimize the influence of the emissivity on the measured temperature. The infrared radiation was measured at two different wavelengths and the ratio of both signals was applied to evaluate the temperature

$$T_R = \left[ \frac{1}{T} - \frac{1}{C_2.(\frac{1}{\lambda_1} - \frac{1}{\lambda_2})} \ln \frac{\varepsilon_1}{\varepsilon_2} \right] \tag{5.26}$$

where $C_2 = \frac{h.c_0}{k}$ is Planck's second radiation constant. It can be seen that the calculated temperature $T_R$ is independent of the emissivity if the spectral emissivities $\varepsilon_1 = \varepsilon(\lambda_1)$ and $\varepsilon_2 = \varepsilon(\lambda_2)$ are equal at the measurement wavelengths $\lambda_1$ and $\lambda_2$ (gray body behavior). In order to fulfill this assumption for different surfaces, the wavelengths were located close together and the wavelength bands are narrow.

In Figure 5.7, the way of placing the fiber optic in to the tool, which was a standard CBN 10, is shown.

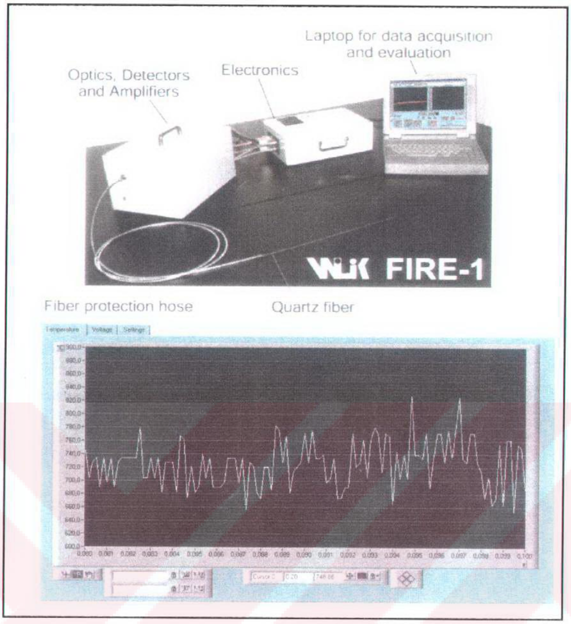


Figure 5.5: Temperature measurement set up.

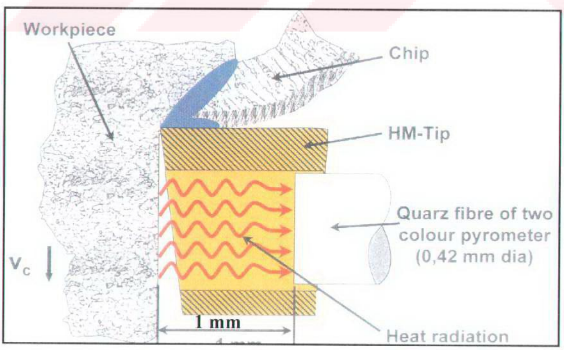


Figure 5.6: Principle of workpiece oriented temperature measurement.

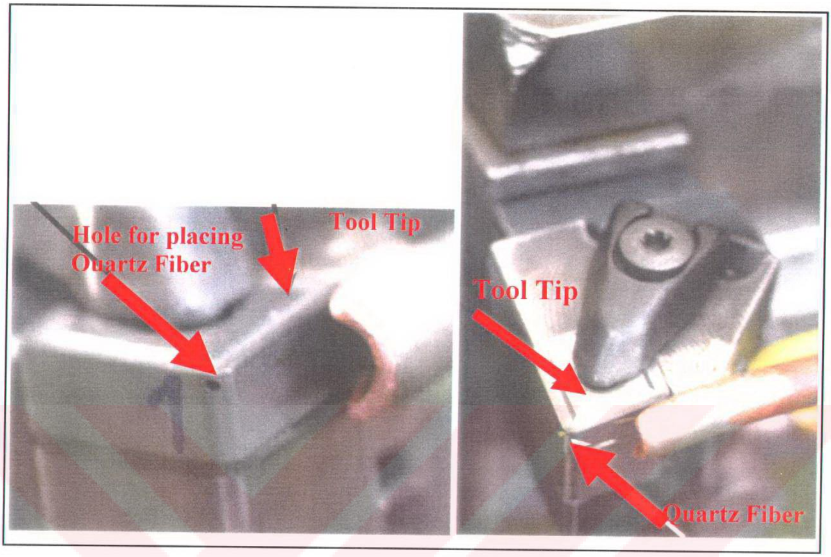


Figure 5.7: Placing of fiber optic into hard metal tip.

In this test feedrate, depth of cut, cutting speed values are 0.10 [mm/rev], 0.2 [mm], 120 [m/min], respectively. Workpiece had thermal conductivity of 42.6 Watt/m.K, density of 7800 kg/m$^3$ and heat capacity of 480 J/kg.C. Tool had thermal conductivity of 43 Watt/m.K, density of 4350 kg/m$^3$ and heat capacity of 1180 J/kg.C. The rake and clearance angles were -20° and 5° respectively. For the finite difference solution, $N_y$, $N_x$, $N_z$ and $N_p$ were set to 8, 24, 8 and 16 respectively. Based on the finite difference model presented above, the predicted average temperature on the rake face was 753 °C and the mean value of the fiber-optic temperature measurement was 725 °C with a standard deviation of 27.5 °C. The experimental temperature measurements are shown in Figure 5.8. And in Figure 5.9 the distribution of temperature measurements are shown. The predicted tool, chip and workpiece temperature fields for these conditions are shown in Figures 5.10-12.

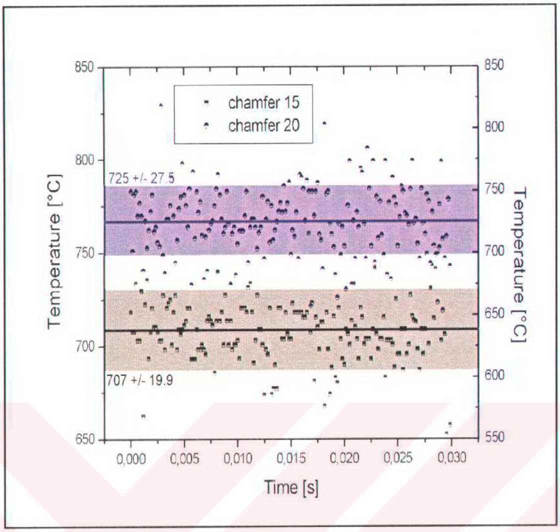


Figure 5.8: Measured temperature results.

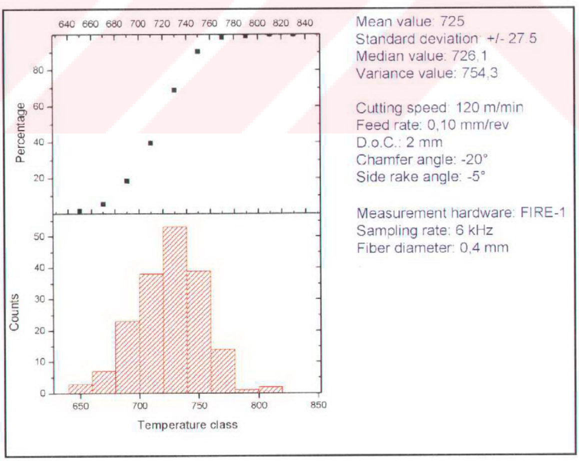


Figure 5.9: Distribution of the temperature measurements.

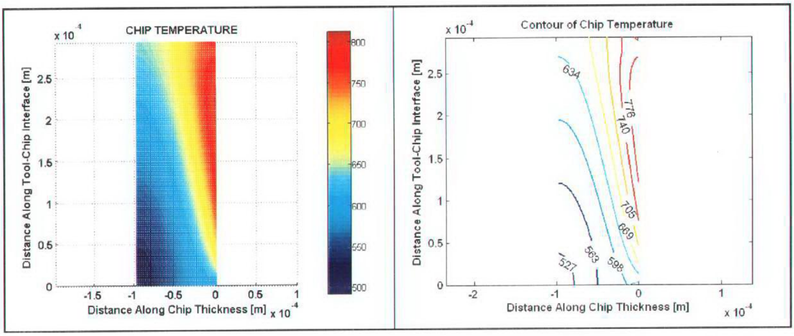


Figure 5.10: Chip temperature field for cutting speed of 120 m/min and rake angle of -20°.

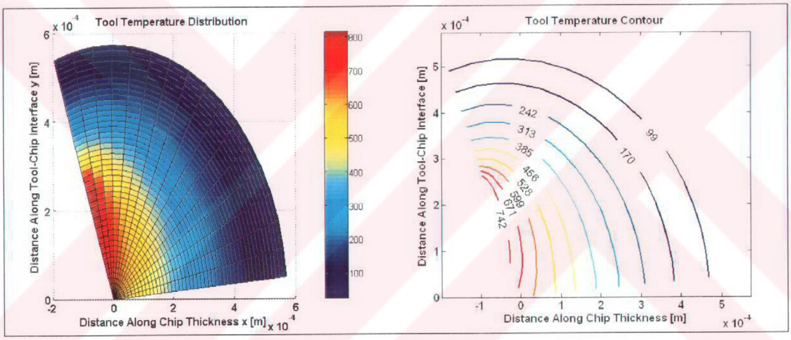


Figure 5.11: Tool temperature field for cutting speed of 120 m/min and rake angle of -20°.

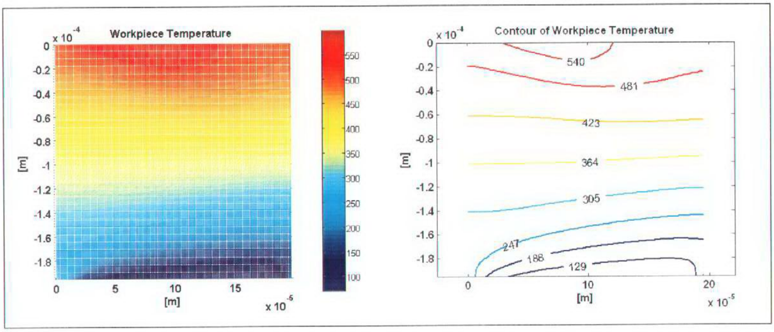


Figure 5.12: Workpiece temperature field for cutting speed of 120 m/min and rake angle of -20°.

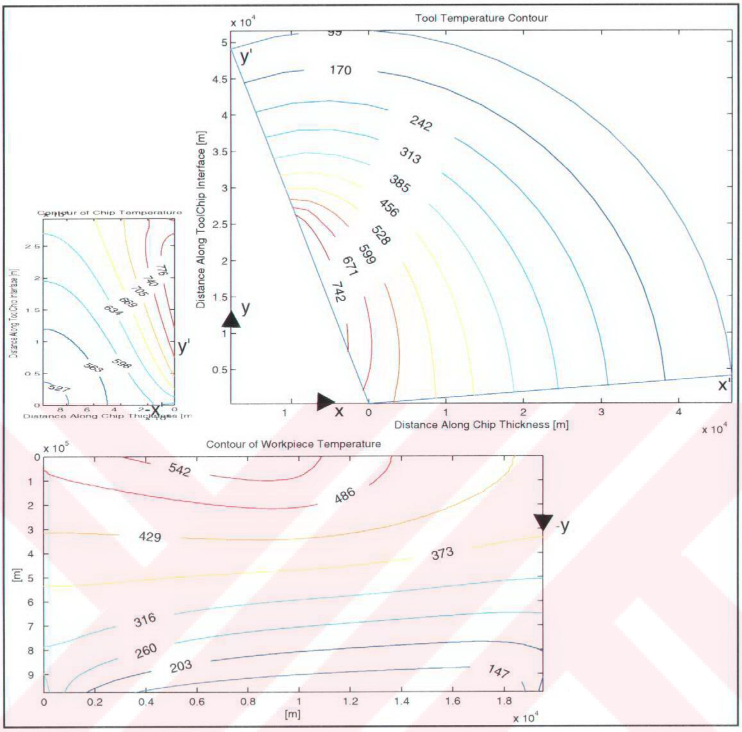


Figure 5.13: Simulation of chip, tool and workpiece temperatures.

Simulations were performed for different rake angle and cutting speed values. Rake face temperature measurements for different rake angle and cutting speed values are shown in Figure 5.14. In Simulation 2, cutting speed is increased to 150 m/min and all other simulation conditions are kept the same as the ones used in Simulation 1. The tool, workpiece, and chip temperature fields created in Simulation 2 are shown in Figures 5.15-17. In Simulation 3, rake angle value is chosen as -15° and all the other cutting conditions including cutting velocity are same as the ones used in Simulation 1. The tool, chip, and workpiece temperature fields created in Simulation 3 are shown in Figures 5.18-20. In order to determine the effect of the velocity increase to the temperature field, rake face temperature variation is plotted for Simulation 1 and Simulation 2. The effect of the increase in cutting speed to the rake face temperature can be seen in Figure 5.21. The effect of the change in rake angle to the rake face temperature can be seen in Figure 5.22. Table 5.1 summarizes the cutting conditions used in simulations.

Table 5.1: Simulation conditions

| | Simulation 1 | Simulation 2 | Simulation 3 |
|---|---|---|---|
| **Workpiece** | 51 Cr V4 (68 HRC) | 51 Cr V4 (68 HRC) | 51 Cr V4 (68 HRC) |
| **Insert** | SECO CBN 10 | SECO CBN 10 | SECO CBN 10 |
| **Cutting Speed** | 120 m/min | 150 m/min | 120 m/min |
| **Feedrate** | 0.10 mm/rev | 0.10 mm/rev | 0.10 mm/rev |
| **$N_x$** | 24 | 24 | 24 |
| **$N_y$** | 8 | 8 | 8 |
| **$N_z$** | 8 | 8 | 8 |
| **$N_p$** | 16 | 16 | 16 |
| **Rake angle** | -20 | -20 | -15 |
| **Clearance angle** | 5 | 5 | 5 |
| **Workpiece thermal conductivity** | 42.6 Watt/m.K | 42.6 Watt/m.K | 42.6 Watt/m.K |
| **Workpiece density** | 7800 kg/m$^3$ | 7800 kg/m$^3$ | 7800 kg/m$^3$ |
| **Workpiece heat capacity** | 480 J/kg.C | 480 J/kg.C | 480 J/kg.C |
| **Tool thermal conductivity** | 43 Watt/m.K | 43 Watt/m.K | 43Watt/m.K |
| **Tool density** | 4350kg/m$^3$ | 4350kg/m$^3$ | 4350kg/m$^3$ |
| **Tool heat capacity** | 1180 J/kg.C | 1180 J/kg.C | 1180 J/kg.C |

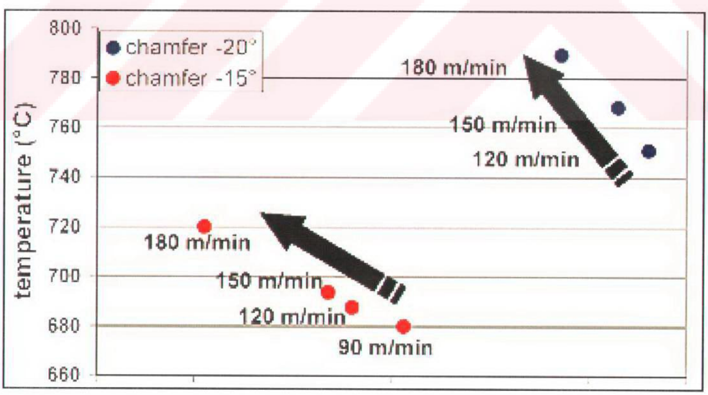


Figure 5.14: Rake face temperature measurements.

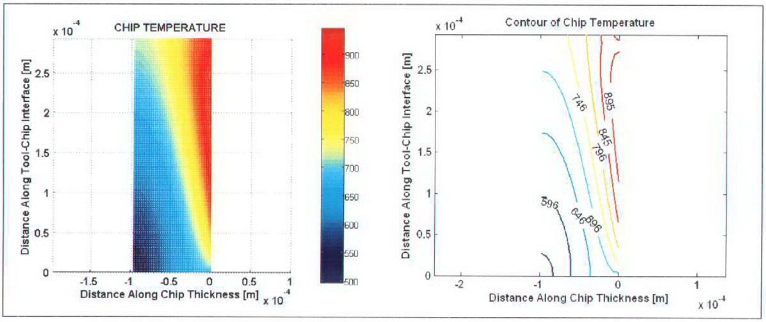


Figure 5.15: Chip temperature field for cutting speed of 150 m/min and rake angle of -20º.

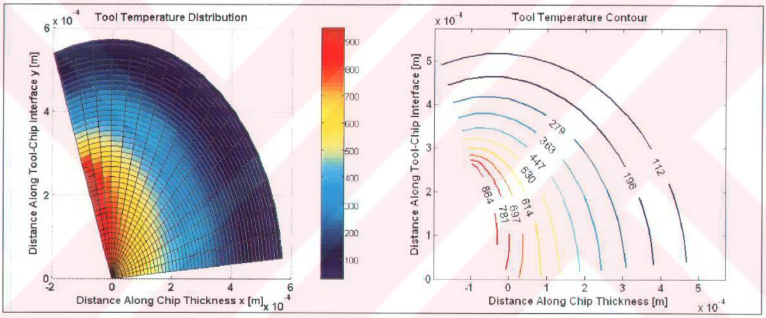


Figure 5.16: Tool temperature field for cutting speed of 150 m/min and rake angle of -20º.

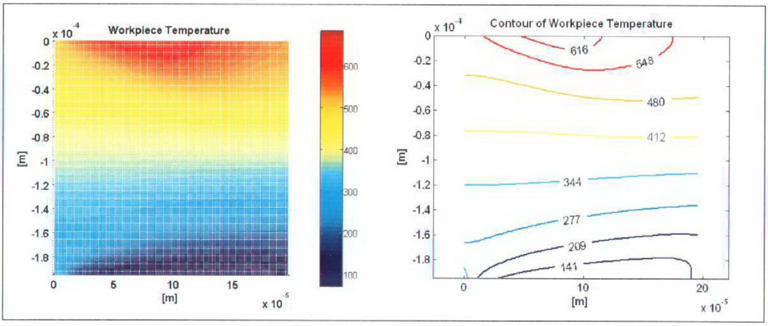


Figure 5.17: Workpiece temperature field for cutting speed of 150 m/min and rake angle of -20º.

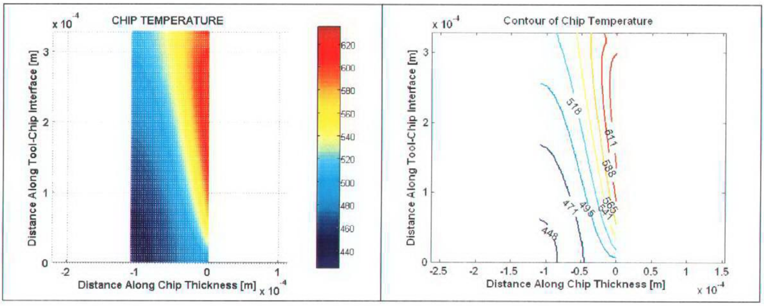


Figure 5.18: Chip femperature field for cutting speed of 120 m/min and rake angle of -15°.

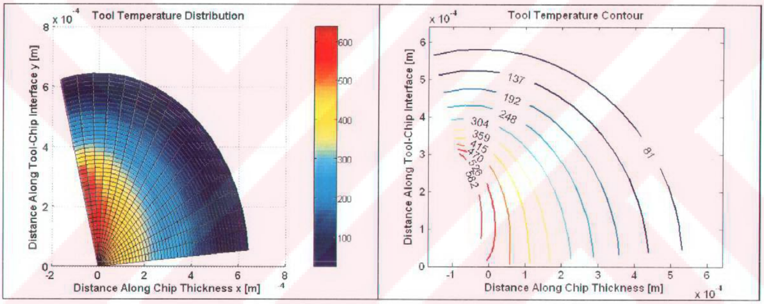


Figure 5.19: Tool temperature field for cutting speed of 120 m/min and rake angle of -15°.

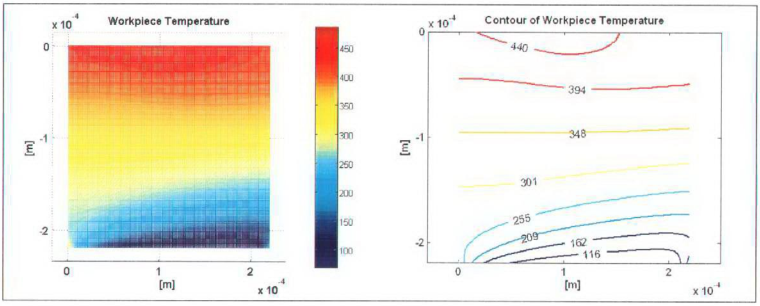


Figure 5.20: Chip temperature field for cutting speed of 120 m/min and rake angle of -15°.

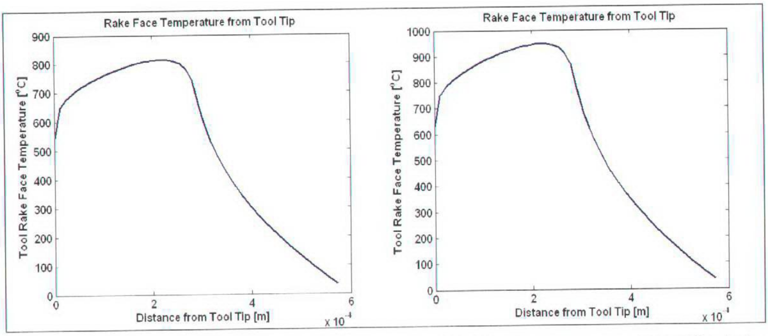


Figure 5.21: Rake face temperature for the rake angle of -20° and cutting speed of a) 120 m/min, b) 150 m/min.

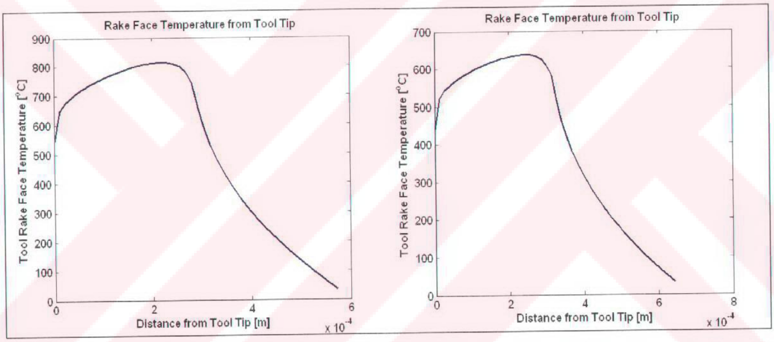


Figure 5.22: Rake face temperature for the cutting speed of 120 m/min and the rake angle of a) -20°, b) -15°.

Average rake face temperature for the cutting speed of 120 m/min and the rake angle of -15° was found to be 658 °C which is very close to the temperature obtained in temperature measurements, in Figure 5.14. Average rake face temperature for the cutting speed of 150 m/min and the rake angle of -20° was found to be 828 °C which is also very close to the one obtained in temperature measurements.

Moreover, it has been seen that when you increase the cutting speed, the temperature on the rake face increases. This is an expected result. Moreover; the decrease in the absolute value of the rake angle causes the temperature to decrease on the rake face. In other words, if a tool with a bigger rake angle is used, the temperature on the rake face increases.

The simulations were performed on various materials in order validate that our model is working on different cutting conditions and materials.

Stephenson and Ali [38] measured temperature during the continuous turning of Al2024-T351 tubes by using a tool-chip thermocouple method. The tool was standard C2 WC tool. The first set of the experimental tests was performed by continuous cutting and the average measured temperature was 280 °C. In this test, cutting speed, feed per revolution, cutting force, feed force and cut chip thickness were 1.36 m/s, 0.165 mm, 573 N, 329 N and 0.333 mm. The width of cut was 2.54 mm. The rake and inclination angles were zero. Based on the previous experiments, they assumed that the chip-tool contact length was given to be 1.5 times the cut chip thickness. Simulation was performed for this cutting conditions using workpiece conductivity, density and thermal capacity of 177 W/ (m.K), 2700 kg/m$^3$, 613 J/(kg-C), respectively, for Al2024-T351. Tool conductivity, density and thermal capacity were 28.4 W/m-K, 11100 kg/m$^3$, 276 J/(kg-C), respectively. The shear angle was determined from the chip ratio as 26.4°. The friction angle was determined as 29.8° from the measured cutting and feed force values. The temperature rise due to the shear was calculated as 215 °C from Equation 5.15. For the finite difference solution, $N_y$, $N_p$ and $dB_{max}$ were set to 10, 8 and 3%, respectively. The predicted steady-state average temperature was found to be 283 °C, which is very close to 280 °C measured by Stephenson and Ali. The results of their temperature measurements are shown in Figure 5.23. The temperature fields of the chip, tool, and workpiece are illustrated in Figures 5.24-26. The maximum tool temperature is predicted to be about 370 °C and it occurs at about 0.4 mm away from the cutting edge. The total chip contact length is about 0.525 mm, and the uncut chip thickness is about 0.165 mm.

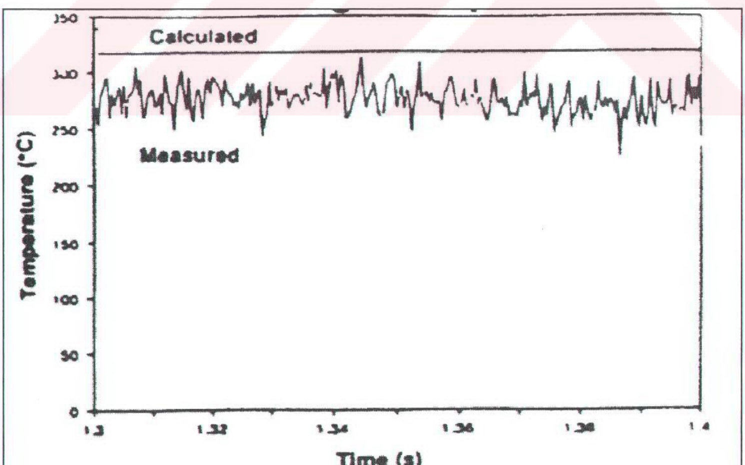


Figure 5.23: Al2024 average rake face temperature measurement, adopted from Stephenson and Ali [38].

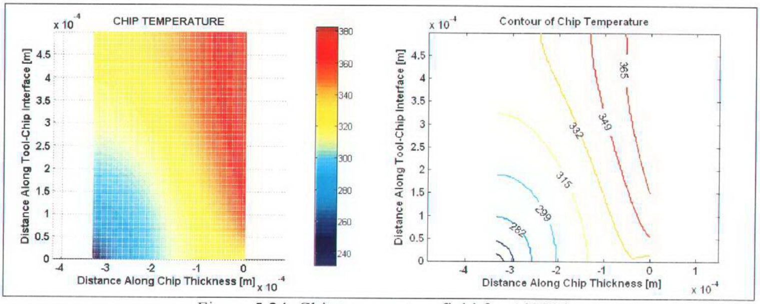


Figure 5.24: Chip temperature field for Al2024.

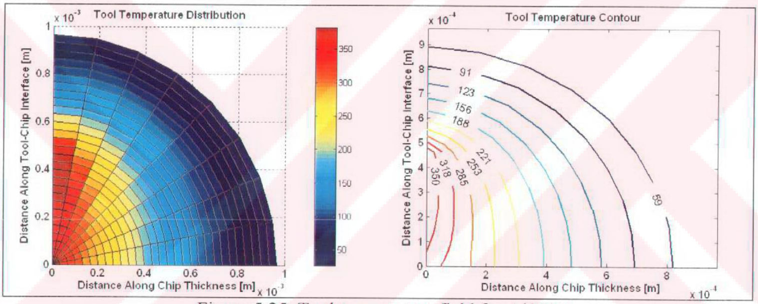


Figure 5.25: Tool temperature field for Al2024.

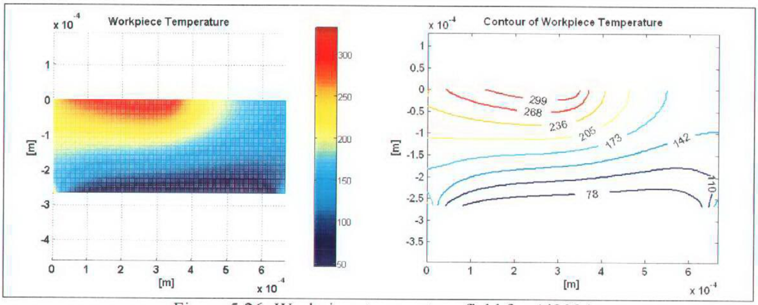


Figure 5.26: Workpiece temperature field for Al2024.

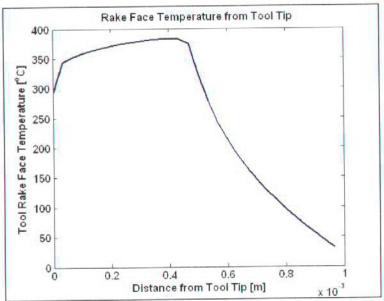

Figure 5.27: Rake face temperature from tool tip.

Thus, in order to simulate temperature generated in hard turning operation, instead of using complex analytical methods or finite element methods, which require accurate representation of material's constitutive properties during machining, using the finite difference method is more advantageous since finite difference models are easier to code and usually solve faster. The time spent to coding is usually longer and a bigger source of error than the time spent to running, so naturally a simpler approach to discretization is a good thing. On a uniform rectangular mesh, it is hard to beat finite difference approximations for simplicity.

# Chapter 6

# CONCLUSION

The objective of the thesis is to analyze the mechanical and thermal aspects of the hard turning process in detail. First of all, a mechanistic approach was proposed for predicting cutting forces in hard turning process. Calibration process was performed for finding cutting force coefficients used in differential chip load and differential cutting force calculation. After differential cutting forces were calculated they were transformed into the measurement coordinate frame and integrated. In the last step of cutting force model the predicted cutting forces were compared with the experimental measurements for the model validation purposes. In general, they showed good agreements in the magnitudes and in the trends.

A process model was developed for prediction of dynamic cutting forces and surface errors in hard turning. Dynamic deflections in the cutting tool were taken into consideration and dynamic chip load was calculated. By using dynamic chip load, dynamic cutting forces were predicted. In order to validate the accuracy of the dynamic model, the surface profile of the workpiece was predicted and compared with the measured surface profile. The results showed that the model is working properly.

A numerical model based on finite difference method was presented for the predictions of steady-state tool, chip and workpiece temperature fields. Simulations were performed under various cutting conditions. Simulated average rake face temperature values were also compared with the experimental Fiber-optic Ratio Pyrometer measurements, they showed good agreements. The simulation of steady state and temperature distribution at the tool rake face has two important uses in high speed machining of metals. The tool should not be used close to and beyond the diffusion and bonding limits of materials used in the specific tool grade. If the tool experiences temperature beyond this limit, it rapidly wears. Hence, the cutting conditions must be selected in such a way that the predicted temperature does not exceed this limit. The proposed algorithm can be utilized in selecting cutting speed, feedrate and tool rake and clearance angles in order to avoid excessive thermal loading of the tool, hence reducing the edge chipping and accelerated wear of the cutting tools.

Possible enhancements to this research will be including the prediction of residual stresses formed on the surface. The author has performed considerable amount of research on this subject. The algorithm for calculation of residual stresses due to thermal and mechanistic loads has been generated. The computer code ending up with residual stresses on the surface has been written, but because of the time limitations it can not be debugged and improved properly. Thus it is left as a future research subject.

It is hoped that this research may shed some more lights on better understanding the physics of the hard turning process. It is also anticipated that the mathematical modeling techniques help researchers and production engineers as tools for selecting the feasible process parameters for achieving higher quality products with shorter cycle-times in hard turning processes.

**BIBLIOGRAPHY**

[1] W. Koenig, A. Berktold, K. F. Koch, Turning versus Grinding-A Comparison of Surface Integrity aspects and Attainable Accuracies, Annals of CIRP, Vol. 42/1, pp. 39-43,1993.

[2] W. Koenig, R. Komanduri, H. K. Tonshoff, and G., Ackershott, Machining of Hard Materials, Annals of CIRP, Vol. 33/2, pp. 417-427, 1984.

[3] W. Koenig, M. Klinger, R. Link, Machining Hard Metals with Geometrically Defined Cutting Edges-Field of Applications and Limitations, Annals of CIRP, Vol. 39/1, pp. 61-64, 1990.

[4] H. K. Tonshoff, C. Arendt, and R. Ben Amor, Cutting of Hardened Steels, Annals of CIRP, Vol. 49/2, pp. 547-566, 2000.

[5] T. J. Ko, and H.S. Kim, Surface Integrity and Machinability in Intermittent Hard Turning, Advance Manufacturing Technology, Vol. 18, pp.168-175, 2001.

[6] C. Scheffer, H. Kratz, P. S. Heyns, and F. Klocke, Development of a Tool Wear-Monitoring System for Hard Turning, International Journal of Machine Tools & Manufacture, Vol.43, pp. 973-985, 2003.

[7] N. Narutaki, and Y. Yamane, Tool Wear and Cutting Temperature of CBN Tools in Machining of Hardened Steels, Annals of CIRP, Vol. 28/1, pp. 23-28, 1979.

[8] K.F. Koch, Technologie des Hochprazisions Hartdrehen, Dissertation RWTH Aachen, 1996.

[9] E.G. Ng, D.K. Aspinwall, D. Brazil, J. Managhan, Modeling of Temperature and Forces when Orthogonally Machining Hardened Steel, International Journal of Machine Tools and Manufacture, Vol. 39, pp. 885-903, 1999.

[10] J. Y. Wang, and C. R. Liu, The Effect of Tool Flank Wear on the Heat Transfer, Thermal Damage and Cutting Mechanics in Finish Hard Turning, Annals of CIRP, Vol. 48/1, pp. 53-58, 1999.

[11] M. A. Davies, Y. Chou, and C. J. Evans, On Chip Morphology, Tool Wear and Cutting Mechanics in Finish Hard Turning, Annals of CIRP, Vol. 45/1, pp. 77-82, 1996.

[12] M. C. Shaw, Chip Formation in Machining of Hardened Steel, Annals of CIRP, Vol. 42/1, pp. 29-33, 1993.

[13] Y. K. Chou, and H. Song, Tool Nose Radius Effects on Finish Hard Turning, Journal of Materials Processing Technology, Vol. 148, Issue 2, pp. 259-268, 2004.

[14] G. Poulachon, B. P. Bandyopadhyay, I. S. Jawahir, S. Pheulpin and E. Seguin, Wear Behavior of CBN Tools While Turning Various Hardened Steels, Wear, Vol. 256, Issues 3-4, pp. 302-310, 2004.

[15] J. Rech, and A. Moisan, Surface Integrity in Finish Hard Turning of Case-hardened Steels International Journal of Machine Tools and Manufacture, Vol. 43, Issue 5, pp. 543-550, 2003.

[16] X. J. Ren , Q. X. Yang , R. D. James, and L. Wang, Cutting Temperatures in Hard Turning Chromium Hardfacings with PCBN Tooling, Journal of Materials Processing Technology, Vol. 147, Issue 1, pp. 38-44, 2004.

[17] A. G. Mamalis, A. S. Branis, and D. E. Manolakos, Modelling of Precision Hard Cutting Using Implicit Finite Element Methods, Journal of Materials Processing Technology, Vol. 123, Issue 3, pp. 464-475, 2002.

[18] K. F. Ehman, S. G. Kapoor, R. E. DeVor, and I. Lazoglu, Machining Process Modeling: A Review, Journal of Manufacturing Science and Engineering, Transactions of ASME, Vol. 119, pp. 655-663, 1997.

[19] C. A. Van Luttervelt, T. H. C. Childs, I. S. Jawahir, F. Klocke, P. K. Venuvinod, Present Situation and Future Trends in Modeling of Machining Operations, Annals of CIRP, Vol. 47/2, pp. 578-626, 1998.

[20] S.A. Tobias, and W. Fishwick, The Chatter of Lathe Tools under Orthogonal Cutting Conditions, Transactions of ASME, Vol. 80, pp. 1079-1088, 1958.

[21] J. Tlusty, and M. Polacek, The Stability of Machine Tools Against Self Excited Vibrations in Machining, International Research in Production Engineering, ASME, pp. 465-474, 1963.

[22] I. Lazoglu, F. Atabey, and Y. Altintas, Dynamics of boring processes: Part Ill-time domain modeling, International Journal of Machine Tools and Manufacture, Vol, 42, n 14, pp. 1567-1576, 2002.

[23] K. J. Trigger, and B. T. Chao, An Analytical Evaluation of Metal Cutting Temperatures, Transactions of ASME, pp. 57-68, 1951.

[24] E. G. Loewen, and M. C. Shaw, Analysis of Cutting-Tool Temperatures, Transactions of ASME, Journal of Engineering for Industry, Vol. 80, pp. 321-329, 1958.

[25] E. Usui, T. Shirakashi, and T. Kitagawa, Analytical Prediction of Three Dimensional Cutting Process, Part 3: Cutting Temperature and Crater Wear of Carbide Tool, Transactions of ASME, Journal of Engineering for Industry, Vol. 100, pp. 236-243, 1978.

[26] J. Tlusty, and E. Orady, Effect of Thermal Cycling on Tool Wear in Milling, 9$^{th}$ NAMRC Conf., Penn. State University, 1981.

[27] A. J. R. Smith, and E. J. A. Armarego, Temperature Prediction in Orthogonal Cutting with a Finite Difference Approach, Annals of CIRP, pp. 9-16, 1981.

[28] H. Ren, Y. Altintas, Mechanics of Machining with Chamfered Tools, Transactions of ASME, Journal of Manufacturing Engineering and Science, Vol. 122, pp. 650-659, 2000.

[29] P. L. B. Oxley, Mechanics of Machining: An Analytical Approach to Assessing Machinability, Ellis Horwood Ltd., 1989.

[30] M. Shatla, Y. C. Yen, O. Castellanos, L. Menegardo, and T. Altan, Prediction of Cutting Forces, Temperatures and Stresses from Flow Stress Data and Cutting Conditions-Research in Progress, Proceedings of Second CIRP International Workshop on Modeling of Machining Operations, Ecole Centrale De Nantes, Nantes France, January 25-26, 1999.

[31] J. S. Strenkowski, and K-J. Moon, Finite Element Prediction of Chip Geometry and Tool/Workpiece Temperature Distributions in Orthogonal Metal Cutting, Transactions of ASME, Journal of Engineering for Industry, Vol. 112, pp. 313-318, 1990.

[32] V. A. Sukaylo, A. Kaldos, G. Krukovsky, F. Lierath, T. Emmer, H. J. Pieper, J. Kundrak, and V. Bana, Development and Verification of a Computer Model for Thermal Distortions in Hard Turning, Journal of Materials Processing Technology, In Press, Corrected Proof, Available online 2 July 2004.

[33] Y. Huang, and S. Y. Liang, Cutting Forces Modeling Considering the Effect of Tool Thermal Property—Application to CBN Hard Turning, International Journal of Machine Tools and Manufacture, Vol. 43, Issue 3, pp. 307-315, 2003.

[34] R. Radulescu, and S. G. Kapoor, An Analytical Model for Prediction of Tool Temperature Fields during Continuous and Interrupted Cutting, Transactions of ASME, J. of Engineering for Industry, Vol. 116, pp. 135-140, 1994.

[35] T. C. Jen, and A. S. Lavine, Prediction of Tool Temperatures in Cutting, Proc. 7th Int. Symposium on Transport Phenomena in Manufacturing, pp. 211-216, 1994.

[36] A. A. O. Tay, A Review of Methods of Calculating Machining Temperature, Journal of Materials Processing Technology, Vol. 36, pp. 225-257, 1993.

[37] G. Boothroyd, Temperatures in Orthogonal Metal Cutting, Proceedings of the Institution of Mechanical Engineers, Vol. 177, no.29, pp. 789-803, 1963.

[38] D. A. Stephenson, and A. Ali, Tool Temperatures in Interrupted Metal Cutting, Transactions of ASME, Journal of Engineering for Industry, Vol. 114, pp. 127-136, 1992.

[39] E. K. Henriksen, Residual Stresses in Machined Surfaces, Transactions of the ASME, Vol. 73, pp. 69-76, 1951.

[40] K. Okushima, and Y. Kakino, Residual Stress Produced by Metal Cutting, Annals of CIRP, Vol. 20, nol,pp. 13-14, 1971.

[41] C. R. Liu, and M. M. Barash, Variables Governing Patterns of Mechanical Residual Stresses in a Machined Surface, Journal of Engineering for Industry, Vol. 104, pp. 257-264, 1982.

[42] J. E. Merwin, K. L. Johnson, Analysis of Plastic Deformation in Rolling Contact, Proceedings of Mechanical Engineering Institution, Vol. 177, pp. 676-690, 1963.

[43] Y. Jiang, H. Sehitoglu, An Analytical Approach to Elastic Plastic Stress Analysis of Rolling Contact, Journal of Tribology, Vol. 116, pp. 577-587, 1994.

[44] Y. Matsumoto, D. W. Wu, Effect of Hardness on Residual Stresses in Orthogonal Machining of AISI 4340 Steel, Journal of Engineering for Industry, August 1990, Vol. 112, pp. 245-252.

[45] D. Y. Jang, A. Seireg, Dynamic Simulation for Predicting Surface Roughness in Turning, American Society of Mechanical Engineers, Design Engineering Division DE, Vol. 18-2, pp. 31-36, 1989.

[46] D. Y. Jang, A. Seireg, A Model for Predicting Residual Stresses in Metal Cutting, Proceedings of the Japan International Tribology Conference, pp. 439-444, 1990.

[47] A. J. Shih, Finite Element Simulation of Orthogonal Metal Cutting, Journal of Engineering for Industry, Vol. 112, pp. 84-93, 1995.

[48] S. Mittal, C. R. Liu, Method of Modeling Residual Stresses in Super Finish Hard Turning, Wear, Vol. 218, no 1, pp. 21-33, 1998.

[49] M. Mahdi, and L. Zhang, Applied Mechanics in Grinding-VI. Residual Stresses and Surface Hardening by Coupled Thermo-Plasticity and Phase Transformation, International Journal of Machine Tools & Manufacture Vol. 38, pp. 1289-1304, 1998.

[50] X. Chen, W. B. Rowe, D. F. McCormack, Analysis of the Transitional Temperature for Tensile Residual Stress in Grinding, Journal of Materials Processing Technology, Vol. 107, pp. 216-221, 2000.

[51] D. G. Walsh, A. A. Torrance and J. Tiberg, Analytical Evaluation of Thermally Induced Residual Stresses in Ground Components, Proceedings of Instn Mechanical Engineers, Vol. 217, Part C: J. Mechanical Engineering Science.

[52] J. D. Thiele, S. N. Melkote, R. A. Peascoe, and T. R. Watkins, Effect of Cutting-Edge Geometry and Workpiece Hardness on Surface Residual Stresses in Finish Hard Turning of AISI 52100 Steel, Transactions of the ASME, Vol. 122, 2000.

[53] C. R. Liu, Y. B. Guo, Finite Element Analysis of the Effect of Sequential Cuts and Tool-Chip Friction on Residual Stresses in a Machined Layer, International Journal of Mechanical Sciences, Vol. 42, pp. 1069-1086, 2000.

[54] R. M'Saoubi, J. C. Outeiro, B. Changeux, J. L. Lebrun, and A. Morafo Dias, Residual Stress Analysis in Orthogonal Machining of Standard and Resulfurized AISI 316L Steels, Journal of Materials Processing Technology, Vol. 96, pp. 225-233, 1999.

[55] K. Jakabus, R. E. DeVor, S. G. Kapoor, Machining-Induced Residual Stress: Experimentation and Modelling, Transactions of the ASME, Vol. 122, 2000.

[56] C. Shet, X. Deng, Residual Stresses and Strains in Orthogonal Metal Cutting, International Journal of Machine Tools & Manufacture, Vol. 43, pp. 573-587, 2003.

[57] Y. Altintas, Manufacturing Automation: Metal Cutting Mechanics, Machine Tool Vibrations, and CNC Design, Cambridge University Press, 2000.

[58] E. J. A. Armarego, Material Removal Processes - An Intermediate Course, Department of Mechanical and Manufacturing Engineering, The University of Melbourne.

# VITA

Kivilcim Buyukhatipoglu completed the high school in Gazi Anadolu Lisesi, Ankara, in 1998. She received her B. Sc. Degree in Mechanical Engineering from Middle East Technical University (METU), Ankara, in 2002. Since 2002, she is in the M. Sc program in Mechanical Engineering at Koc University as a teaching/research assistant.